Published for SISSA by Springer

Received: January 29, 2019
Accepted: March 25, 2019
Published: March 26, 2019

Asymmetric heavy-quark hadroproduction at LHCb: predictions and applications

Rhorry Gauld,[a] **Ulrich Haisch**[b] **and Benjamin D. Pecjak**[c]

[a] *Nikhef Theory Group,*
Science Park 105, 1098 XG Amsterdam, The Netherlands
[b] *Max Planck Institute for Physics,*
Föhringer Ring 6, 80805 München, Germany
[c] *Institute for Particle Physics Phenomenology, Durham University,*
Durham DH1 3LE, U.K.

E-mail: rgauld@nikhef.nl, haisch@mpp.mpg.de, ben.pecjak@durham.ac.uk

Abstract: We present a phenomenological analysis of asymmetric bottom- and charm-quark production within the LHCb acceptance relevant for pp collisions at $\sqrt{s} = 13\,\text{TeV}$. Predictions are provided for both anti-k_t bottom- and charm-jet pairs, which are kept differentially with respect to the invariant mass of the jet pair. It is quantified how data in this region can provide sensitivity to the couplings of the Z boson to heavy quarks, and we investigate what precision is needed to compete with LEP. We also discuss how asymmetry and rate measurements can provide constraints on a particular class of new-physics models, which contains gauge bosons with small/moderate couplings to light/heavy quarks and masses of the order of 100 GeV. Predictions are obtained including all relevant QCD and QED/weak contributions up to next-to-leading order, which have been implemented in a Fortran code which allows to directly compute the asymmetric cross sections. We provide all relevant analytic formulas for our computations.

Keywords: QCD Phenomenology

ArXiv ePrint: 1901.07573

https://doi.org/10.1007/JHEP03(2019)166

JHEP03(2019)166

Contents

1 Introduction

The production of bottom and charm quarks at high-energy colliders is a topic of considerable interest. While not directly observed, these quarks fragment into unstable bottom and charm hadrons with a typical mean lifetime of 10^{-12} s. As a consequence of the short but finite lifetime, bottom and charm hadrons decay within the detector at a location which is displaced from the primary collision point. This distinct experimental signature can be used to associate the production of a particle jet in the collision with that originating from a heavy quark, or to improve the efficiency for exclusively reconstructing the heavy-flavour hadron, which in turn has allowed detailed studies of heavy-quark production.

A relevant example is the pair-production of bottom- and charm-quarks in e^+e^- collisions in the vicinity of the Z pole, as studied at both LEP and SLC. Precision measurements

JHEP03(2019)166

of both the production rates and the asymmetries in angular distributions of the produced heavy-quarks has allowed to perform precision tests of the Standard Model (SM), and has led to the most stringent constraints on the coupling structure of the Z boson to all quarks but the top quark [1]. Similar studies of the angular asymmetries in heavy-quark production have also been carried out at hadron colliders. In $p\bar{p}$ collisions at the Tevatron, a measurement of the asymmetry in b-quark pair production has been performed for B-hadrons by the DØ collaboration [2], and also for bottom-quark jet (b-jet) pairs by the CDF collaboration [3]. A measurement of the b-jet pair asymmetry has also been achieved by the LHCb collaboration in pp collisions at the LHC [4].

The asymmetric hadroproduction of heavy-quarks provides important information as compared to what is accessible in e^+e^- collisions. First, the production mechanisms are entirely different in these collisions, and therefore unique information is provided in hadron collisions. In addition, a measurement of the asymmetry can be performed differentially in the invariant mass of the $b\bar{b}$ system across a large range of values. This information allows to test a number of new-physics scenarios which are not accessible in e^+e^- collisions, and there have been a number of relevant phenomenological studies both in the SM and beyond (cf. [5–14] for instance). It is, however, important to note that the prediction and measurement of heavy-quark asymmetries at hadron colliders also come with a number of challenges. Experimentally it is necessary to account for the effects of pile-up, and to suppress the extremely large background contributions from light-flavour jet production. In addition, the absolute value of the predicted asymmetry is typically quite small. This is mainly a consequence of the large suppression introduced by the symmetric gluon-fusion subprocess for heavy-quark pair production. On the theoretical side, the evaluation of QCD corrections (which are dominant) to heavy-quark production are more complicated at hadron colliders because all external particles are coloured. Obtaining predictions are furthermore computationally more intensive, as the partonic cross sections have to be convoluted with parton distribution functions (PDFs).

The purpose of this work is to provide robust predictions for both bottom- and charm-quark jet-pair production in pp collisions at the 13 TeV LHC in the forward direction. There are at least two motivations for focussing on this specific kinematic region. First, the forward regime provides unique opportunities to measure heavy-quark asymmetries at the LHC, because of the increased asymmetry between q and $\bar{q}$ PDFs present when these partons carry large energy fractions, and the reduced dilution of the symmetric gluon-fusion contribution. Second, the LHCb experiment is a forward detector [15] and able to perform both charge- and flavour-tagging of heavy-quark jets [4, 16]. In fact, the recent LHCb measurement of the $Z \to b\bar{b}$ production cross section [17] indicates that finely binned heavy-quark asymmetry measurements in the Z-pole region should be possible as well. As we will show in this article, the latter point is of relevance as there is a long-standing tension between the measured and the SM value of the $b\bar{b}$ forward-backward asymmetry in e^+e^- collisions [1]. It is also discussed how measurements of bottom- and charm-quark pair production can provide constraints on new-physics models, which contain gauge bosons with masses of around 100 GeV and small/moderate couplings to light/heavy quarks.

JHEP03(2019)166

The remainder of the paper is laid out as follows. In section 2 we provide details of the theoretical set-up that we use to obtain our numerical results. The SM predictions for the cross sections and the asymmetries are given in section 3 and section 4, respectively. Two applications of our results are presented in section 5 and conclude our article. The technical details of our calculations and their numerical implementation can be found in appendix A.

2 Theoretical framework

As discussed in the introduction, the goal of the experimental analysis [4] is to measure an asymmetry in the rapidity distributions of b- and $\bar{b}$-quarks produced in pp collisions. Experimentally, this has been achieved by requiring the presence of two anti-k_t jets [18] which are both charge- (in the presence of a semi-leptonic B decay) and flavour-tagged. This procedure allows to differentiate between b- and $\bar{b}$-quark jets and to construct asymmetric observables. Practically, the asymmetry is measured differentially with respect to the invariant mass of the b- and $\bar{b}$-jet pair system.

The corresponding theoretical predictions for the inclusive process $pp \to Q\bar{Q}X$ with Q referring to either a bottom or charm quark in this work are obtained assuming a standard factorisation theorem [19], whereby the hadron-level cross section can be computed by convoluting the individual partonic cross sections with the relevant PDFs. Theoretical predictions for heavy-quark production can be characterised in terms of the perturbative accuracy of the partonic cross sections according to

$$\mathrm{d}\hat{\sigma} = \sum_{n,\,m} \alpha^n \alpha_s^m \, \mathrm{d}\hat{\sigma}^{(n,\,m)} \,, \tag{2.1}$$

where $\mathrm{d}\hat{\sigma}^{(n,\,m)}$ denotes the coupling-stripped differential partonic cross section and α (α_s) is the QED (QCD) coupling. The leading order (LO) contributions to (2.1) correspond to $n + m = 2$, while the next-to-leading order (NLO) contributions have $n + m = 3$, and so forth. In this work, we include all numerically relevant NLO corrections to the distributions.[1] The technical details of the calculation and implementation of the various contributions to the partonic cross sections are discussed in appendix A. The techniques to obtain NLO corrections to $2 \to 2$ processes are by now standard, and in the case of $pp \to Q\bar{Q}X$ all relevant NLO contributions are known since some time [20–29] (see also references therein for partial results). We therefore refrain from giving NLO expressions for (2.1) in the main text. Instead we provide an overview of the numerical implementation of our calculations in the following, and discuss the details of the various inputs and scheme choices, which are relevant to the numerical predictions provided in this article.

2.1 General set-up

The numerical predictions in this paper are obtained by means of a private Fortran code, which is linked to a number of external libraries: the evaluation of the input PDFs is performed with `LHAPDF` [30], the numerical integration algorithms of `CUBA` [31] are used, and

[1] The tiny $\mathcal{O}(\alpha^3)$ corrections are neglected in our predictions.

JHEP03(2019)166

one-loop scalar integrals are evaluated with `OneLOop` [32, 33]. An important aspect of the implementation of our analytic calculations is that we separate the contributions to the partonic cross sections into parts that are symmetric and asymmetric under interchange of the final-state heavy quarks. The numerical integration of the symmetric and asymmetric contributions can therefore be performed independently. This approach significantly improves the stability of the numerical integration of the asymmetric cross sections, as only the asymmetric contributions of the partonic cross sections are integrated and the numerical adaption of the integration is specifically optimised for these contributions.

The mass of the considered heavy quark is included in our calculations, and we therefore work in a scheme with $N_F = 4\,(3)$ massless quarks for the bottom-quark (charm-quark) predictions. The $\mathcal{O}(\alpha_s^3)$ corrections to the symmetric cross sections are obtained with the matrix elements [20] implemented in `POWHEG BOX` [34]. The calculation of the weak box-diagram corrections of $\mathcal{O}(\alpha\alpha_s^2)$ have instead been obtained using `MadLoop` [35] as part of the loop-induced module [36] available in `MadGraph5_aMC@NLO` [37].[2] All other contributions have been computed with the aid of `FeynArts` [39] and `FormCalc` [40], and the relevant analytic formulas for the asymmetric contributions to the partonic cross section are collected in appendix A. In these cases, we have used the technique of phase-space slicing [41] or dipole subtraction [42] to regulate the explicit (implicit) divergences present in the virtual (real) phase-space.

We add that differential $\mathcal{O}(\alpha_s^4)$ results have been first presented for top-quark production in [43], as well as for massless partons to leading colour in [44]. At present, a calculation of b-tagged jets (either massive or massless) is instead not available. However, it can be expected that such predictions will become available in the future when issues related to numerical stability or flavour-tagging of subtraction terms in the next-to-next-to-leading order (NNLO) QCD calculations have been resolved.

2.2 Observables

To match the experimental definition of jet observables, we construct anti-k_t jets with a radius parameter $R = 0.5$ and tag them as a Q-jet ($\bar{Q}$-jet) if they contain a Q ($\bar{Q}$), with Q being the heavy quark. Throughout this work, all observables are computed in terms of these flavour-tagged jets. The label "jet" will however be suppressed, meaning for example that the invariant mass of a b- and $\bar{b}$-jet pair will be simply called $m_{b\bar{b}}$. If not stated otherwise, we will always place the following kinematic cuts on the flavour-tagged heavy-quark jets

$$p_{T,Q\,(\bar{Q})} > 20.0\,\text{GeV}\,, \qquad \eta_{Q\,(\bar{Q})} \in [2.2, 4.2]\,, \qquad \phi_{Q\bar{Q}} > 2.6\,. \tag{2.2}$$

referring to these selections as "LHCb kinematic cuts". The requirements on the transverse momentum (p_T) and the pseudorapidity (η) ensure that the jets are reconstructed according to the flavour tagging algorithm in use at LHCb [16]. The cut on the angular separation (ϕ) between the two flavour-tagged jets in the azimuthal plane ensures that the two heavy-quark jets are well separated. This cut therefore avoids configuration which can appear for

[2] Details on this set-up are available on the wiki page [38]. We thank Valentin Hirschi for his assistance with this part of the calculation.

JHEP03(2019)166

instance at $\mathcal{O}(\alpha_s^3)$ where both the Q and $\bar{Q}$ are contained within a single jet (at LO this cannot occur as the heavy quarks are produced back-to-back). The impact of the choice of the angular cut on the predicted asymmetries is discussed in section 4.

The two primary observables of interest are the heavy-quark production cross sections and the corresponding asymmetries. The cross sections are computed differentially in $m_{Q\bar{Q}}$ within the LHCb fiducial region (2.2). The asymmetries are also computed differentially in $m_{Q\bar{Q}}$, and defined according to

$$\frac{\mathrm{d}A}{\mathrm{d}m_{Q\bar{Q}}} = \left(\frac{\mathrm{d}\sigma_S}{\mathrm{d}m_{Q\bar{Q}}}\right)^{-1} \left(\frac{\mathrm{d}\sigma_A}{\mathrm{d}m_{Q\bar{Q}}}\bigg|_{\Delta y>0} - \frac{\mathrm{d}\sigma_A}{\mathrm{d}m_{Q\bar{Q}}}\bigg|_{\Delta y<0}\right) . \tag{2.3}$$

Here $\mathrm{d}\sigma_{S\,(A)}$ refers to the convolution integral of the differential (a)symmetric partonic cross sections with the relevant PDFs, and $\Delta y = y_Q - y_{\bar{Q}}$ is the difference between the rapidities of the Q and the $\bar{Q}$.

2.3 Heavy-quark mass effects

As mentioned above, we retain the effects of the heavy-quark mass throughout our calculations. The following choices for the heavy-quark masses in the on-shell scheme are adopted

$$m_b = 4.75\,\mathrm{GeV}\,, \qquad m_c = 1.5\,\mathrm{GeV}\,. \tag{2.4}$$

These values are broadly consistent with the recommendations of the LHC Higgs Cross Section Working Group [45]. When we provide predictions for either cross sections or asymmetries, we do not consider the uncertainties associated to (2.4). The motivation for this is that the mass corrections within the considered fiducial region are typically small (although not negligible), and the resulting ambiguities are small compared to the scale uncertainties. This statement is corroborated in figure 1 (left), which shows LO differential $b\bar{b}$ cross sections within the LHCb fiducial region (2.2) for different choices of m_b. These distributions are obtained with the `LUXqed15` [46] central PDF set member with factorisation (μ_F) and renormalisation (μ_R) scales set dynamically to $m_{b\bar{b}}$, and the distributions have been normalised to the result obtained with $m_b = 4.75\,\mathrm{GeV}$. As can be seen from the distribution obtained with $m_b = 0$ the mass corrections amount to 3% to 10% within $m_{b\bar{b}} \in [40, 100]\,\mathrm{GeV}$. On the other hand, a variation of m_b in the range $m_b \in [4.5, 5.0]\,\mathrm{GeV}$ results in cross-section changes below the percent level. While this study focuses on the case of symmetric $b\bar{b}$ production within the LHCb fiducial region, similar corrections (although with opposite sign) are observed for asymmetric $b\bar{b}$ production within this region. In the $c\bar{c}$ case, the mass corrections remain always below 2%. We also note that the inclusion of mass effects leads to a positive correction to the symmetric cross section within the LHCb fiducial region, while the inclusive cross section within the same invariant mass region receives negative corrections.

While to achieve precision predictions in the region of $m_{b\bar{b}} \in [40, 100]\,\mathrm{GeV}$ including mass corrections is clearly important, at larger values of $m_{b\bar{b}}$ one could alternatively perform the calculation taking the heavy quarks to be massless. Employing a massless scheme

JHEP03(2019)166

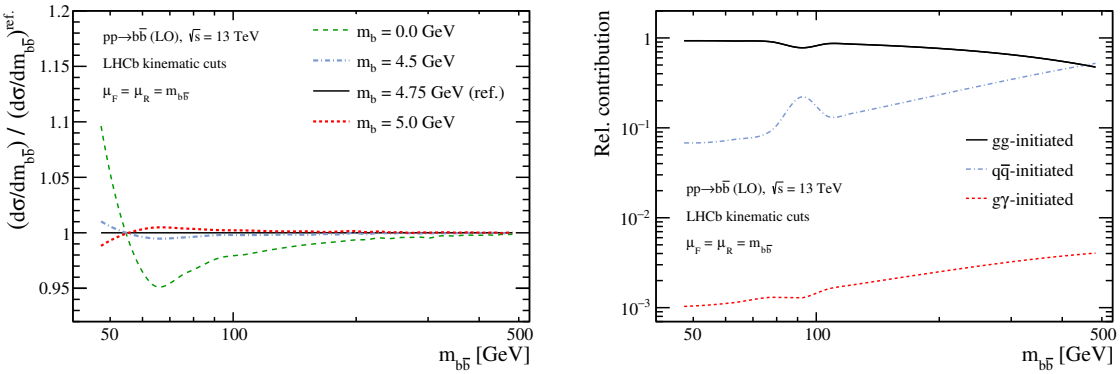

Figure 1. Left: differential cross sections for producing b-jet pairs for different choices of m_b, normalised to the result obtained with $m_b = 4.75\,\text{GeV}$. Right: relative contributions of each partonic channel to the differential cross section for the choice $m_b = 4.75\,\text{GeV}$. The shown results are LO accurate and correspond to pp collisions at $\sqrt{s} = 13\,\text{TeV}$, employing the selections (2.2).

would have the advantage that logarithmic mass corrections could be resummed, but also has some weaknesses. In this context it is important to recall that the measurement is performed by requiring the presence of two well separated flavour-tagged anti-k_t jets according to (2.2). With such kinematic requirements, the phase-space regions where the NLO fixed-order calculation receives large logarithmic corrections (for example, due to the presence of $g \to b\bar{b}$ collinear enhancements) are avoided, and the effects of resumming these types of contributions is therefore typically small.[3] Another consideration is that the prediction of flavour-tagged anti-k_t jets is only infrared (IR)-safe for the massive calculation. Due to the presence of wide-angle $g \to Q\bar{Q}$ splittings of soft gluons, the massless calculation is IR-unsafe [47]. We therefore provide our predictions including the full mass effects up to NLO, such that it is possible that numerical predictions computed with the massive NNLO calculation [48] can be added consistently at a later date. Alternatively one could consider a flavour-tagging algorithm which is IR-safe and achievable experimentally.

2.4 PDFs, input parameters and scale variation

As a baseline PDF set in this work, we use the variant of `NNPDF31_nlo_as_0118` [49] where the charm-quark PDF is generated purely perturbatively. This is a variable flavour number scheme set with $N_F = 5$, which is therefore evolved (both PDFs and α_s) with five active flavours above the b-quark mass threshold. As discussed throughout this section, we deliver predictions for bottom- and charm-quark pair production at NLO including both QCD and QED/weak corrections. For consistency, these predictions should be obtained by convoluting the partonic cross sections with PDFs which have been extracted from a PDF fit including both QCD and QED effects. There are two important points related to the choice of PDFs which we describe below.

[3] It was checked that for the LHCb kinematic cuts (2.2), the contribution from the subprocess $b\bar{b} \to b\bar{b}$ in the massless scheme accounts for only around 1% of the total cross section.

JHEP03(2019)166

First, when calculating $b\bar{b}$ ($c\bar{c}$) production using $N_F = 4\,(3)$ active flavours, there is a mis-match at $\mathcal{O}(\alpha_s^3)$ between the perturbative cross-section calculation and our input PDF set which uses $N_F = 5$. To account for this we include the relevant compensation terms following [50]. Second, our baseline PDF does not include a photon PDF or the effects of a joint QCD-QED evolution [51]. There has recently been quite some activity in precisely determining the photon PDF [46, 52–55] and also a number of studies of electroweak (EW) effects in top-quark pair production have been presented [56–58]. We have studied the impact of the latter two types of contributions for bottom- and charm-quark pair production, and found these effects of very limited importance. This is demonstrated in figure 1 (right) where the contributions of gluon-fusion, quark-annihilation, and gluon-photon scattering to the $b\bar{b}$ cross section are shown. The given predictions are obtained at LO with the `LUXqed15` PDF set using $\mu_F = \mu_R = m_{b\bar{b}}$ and employing the reference cuts (2.2) at the 13 TeV LHC. In the considered invariant mass range, we find that the photon-induced contributions lead to effects at the permille level. Compared to the uncertainty of the total cross section (which is around 10%), these effects are thus entirely negligible.[4] We have therefore chosen to use a PDF set based on NLO QCD which does not include a photon PDF. A consequence of ignoring the mixed QCD-QED evolution effects is to slightly overestimate the uncertainty due to μ_F variation used to assess the theoretical uncertainty of our predictions.

In this work, we use the following input parameters: $m_h = 125\,\text{GeV}$, $m_t = 173\,\text{GeV}$, $M_W = 80.385\,\text{GeV}$, $\Gamma_W = 2.085\,\text{GeV}$, $M_Z = 91.1876\,\text{GeV}$, $\Gamma_Z = 2.4952\,\text{GeV}$ as well as $G_F = 1.16638 \cdot 10^{-5}\,\text{GeV}^{-2}$. Employing this input and including the dominant one- and two-loop universal corrections to the ρ-parameter [59], we have derived the following values for the square of the sine of the weak mixing angle $\sin^2\theta_w = 0.2293$ and the electromagnetic coupling $\alpha = 1/128.55$. For the values of the Cabibbo-Kobayashi-Maskawa (CKM) matrix, we take $|V_{us}| = |V_{cd}| = \sqrt{1-|V_{ud}|^2} = \sqrt{1-|V_{cs}|^2} = 0.23$, $|V_{tb}| = 1$, while all other elements are set to zero. For the evaluation of the $\mathcal{O}(\alpha\alpha_s^2)$ corrections we use a complex mass-scheme [60], accounting for the width effects of the Z boson. In the latter case, the (complex) value of the weak mixing angle is derived from the complex W- and Z-boson masses.

To assess the uncertainty due to missing higher-order corrections, scale variations are performed by changing both μ_F and μ_R independently by a factor of two around a reference scale μ_0, with the constraint that $1/2 < \mu_F/\mu_R < 2$. Predictions are obtained for the two following choices of the reference scale

$$\mu_0 = m_{Q\bar{Q}}\,, \qquad \mu_0 = \overline{E}_{T,Q} = \frac{E_{T,Q} + E_{T,\bar{Q}}}{2}\,, \tag{2.5}$$

corresponding to the invariant mass of the heavy-quark jet pair and the mean transverse energy of the heavy-quark jets, respectively. When observables such as the asymmetry defined in (2.3) or a cross-section ratio between heavy quarks are considered, the scale variations are computed by correlating the scales between numerator and denominator.

To conclude this section, we note that it is straightforward to also provide predictions for stable top quarks with our numerical set-up. The production of top quarks at forward rapidities is of considerable interest [61–63], and there has been significant experimental

[4] The only exception is the ratio of bottom- and charm-quark jet rates which is discussed in section 3.

JHEP03(2019)166

progress towards performing precise forward measurements of this process [64, 65]. However, as only partial event reconstruction is possible, studying the phenomenology of stable top quarks within the LHCb acceptance is not very practical. For a detailed discussion of the leptonic top-quark asymmetries at LHCb, we refer the interested reader to [63].

3 Cross-section predictions

The main goal of this work is to provide reliable predictions for asymmetric heavy-quark production in the fiducial region (2.2). Having a clear understanding of the associated cross sections is, however, an important ingredient of this analysis as well. From the theoretical point of view, it is important to validate the absolute heavy-quark jet rates as well as the shape of the invariant mass distributions, in particular in the region around the Z pole. Experimentally, measurements of the cross sections may give handles on the (charged) flavour-tagging efficiency and the mis-tag rates, as well as providing an important validation of the jet-energy scale and resolution corrections. The differential heavy-quark cross sections may also lead to constraints on new-physics models which contain light gauge bosons, a point we will return to in section 5. The remainder of the current section is dedicated to the study of the symmetric distributions.

3.1 Cross sections

Figure 2 gives our $\sqrt{s} = 13\,\text{TeV}$ predictions for the heavy-quark jet rates within the LHCb acceptance (2.2). The results have been obtained at NLO for both b- (left) and c-jet (right) pairs for the two dynamical references scales (2.5) with the corresponding scale uncertainties shown as error bands. In order to allow to assess the perturbative stability of the predictions, the LO predictions obtained with $\mu_0 = \overline{E}_{T,Q}$ are also displayed. In both cases, the lower panel of the plots shows the distributions normalised to the central NLO prediction obtained with $\mu_0 = m_{Q\bar{Q}}$.

In the figure we have focussed on the region of $m_{Q\bar{Q}} \in [60, 300]\,\text{GeV}$, where the differential cross sections span several orders of magnitude. The scale uncertainties of the NLO distributions are about 10%, which represents a marked improvement with respect to the LO results. We also find that the NLO distributions corresponding to the two scale choices (2.5) lead to consistent results, and tend to lie within the uncertainty bands of the LO distributions. In the region of $m_{Q\bar{Q}} \geq 100\,\text{GeV}$ the cross sections are entirely dominated by the QCD contributions, and there is a 5% to 10% difference between the central values of the NLO results obtained with $\mu_0 = m_{Q\bar{Q}}$ or $\mu_0 = \overline{E}_{T,Q}$. An improvement in the perturbative stability of the predictions in this region would require the inclusion of $\mathcal{O}(\alpha_s^4)$ corrections, either through a fixed-order calculation or by performing resummation (see for example [66]). The fiducial cross sections within the invariant mass bin $m_{Q\bar{Q}} \in [250, 300]\,\text{GeV}$ are approximately 30 pb. Assuming an integrated luminosity of $5\,\text{fb}^{-1}$ and a signal efficiency $\epsilon_{Q\bar{Q}} = 0.6\%$, these numbers imply that a relative statistical uncertainty of about 1% may be achievable with future LHCb data.

LHCb has recently performed a measurement of the process $pp \to Z \to b\bar{b} + \text{jets}$ at $\sqrt{s} = 8\,\text{TeV}$ [17]. This measurement is performed differentially with respect to $m_{b\bar{b}}$ in

JHEP03(2019)166

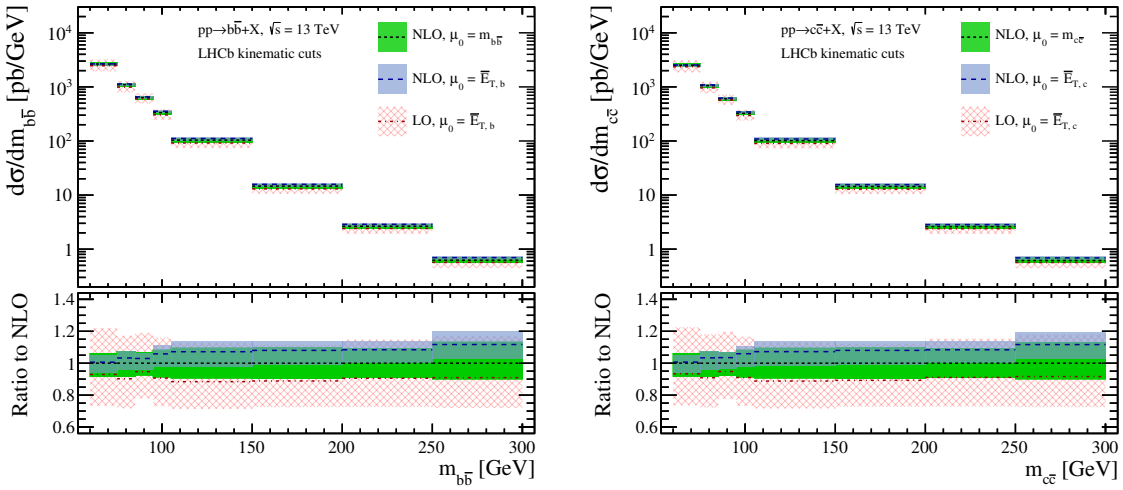

Figure 2. Differential $b\bar{b}$ (left) and $c\bar{c}$ (right) cross sections for pp collisions at $\sqrt{s} = 13\,\text{TeV}$ in the fiducial region (2.2). The NLO distributions employ the two scale choices $\mu_0 = m_{Q\bar{Q}}$ and $\mu_0 = \overline{E}_{T,Q}$, and LO distributions obtained with $\mu_0 = \overline{E}_{T,Q}$ are also shown. The lower part of each panel displays the distributions normalised to the central NLO prediction obtained with $\mu_0 = m_{Q\bar{Q}}$.

bins of width 4 GeV in the Z-pole region, suggesting that future measurements of inclusive heavy-quark pair production will also be possible with similarly fine binning. In figure 3 we provide predictions for both bottom (left) and charm (right) jet-pair production, focussing on the invariant-mass region of $m_{Q\bar{Q}} \in [60, 120]\,\text{GeV}$. Besides the total rates also spectra of the various subprocesses are shown. At LO we display the purely QCD (α_s^2) and EW (α^2) contributions, while at NLO we have chosen to depict various combinations of mixed QCD-EW corrections. When considering the EW corrections to the LO QCD processes ($\alpha\alpha_s^2$) only the values of the NLO coefficient is displayed, where we have separated the impact of the QED and weak corrections. The QED corrections in this case are negative, and thus the absolute values of the NLO coefficient are shown. In the case of the QCD corrections to the LO EW processes ($\alpha^2\alpha_s$) the sums of the LO and NLO coefficients are given, where we have also displayed the result when including only initial-state radiation (ISR) from QCD (labelled as ISR only).

The LO QCD contributions are by far dominant, while the LO EW contribution only becomes relevant (reaching roughly 10%) in the region of $m_{Q\bar{Q}} \in [85, 95]\,\text{GeV}$. The QED corrections to the LO QCD process are negative and more important in the case of charm-quark production,[5] where these effects amount to half a percent of the total cross section. For both bottom- and charm-quark production, the weak corrections are negligibly small. The QCD corrections to the LO EW process have a more important impact on the obtained results. This is primarily due to the contribution of hard QCD corrections to the heavy-quark lines, where an emitted gluon is not reconstructed as part of the heavy-flavour jet. A consequence of such resonantly enhanced events which lose energy via the emission of such

[5]This contribution is dominated by the QED correction to the $gg \to Q\bar{Q}$ subprocess, which is proportional to the squared electric charge of the heavy quark.

JHEP03(2019)166

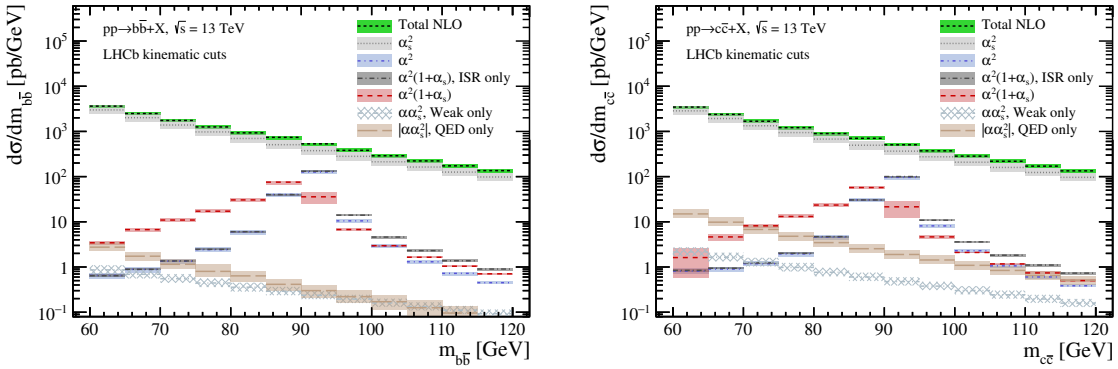

Figure 3. Same as figure 2 but restricted to invariant masses $m_{Q\bar{Q}} \in [60, 120]$ GeV. Besides the full NLO results various individual contributions are shown. See text for further details.

a hard gluon results in a shift of the Z peak to lower $m_{Q\bar{Q}}$ values. For $m_{Q\bar{Q}} \in [85, 95]$ GeV, the corresponding numerical effect amounts to several percent at the cross-section level.

As a final comment to figure 3 (right), we note that the scale variation present for the $c\bar{c}$ prediction of $\mathcal{O}(\alpha^2\alpha_s)$ in the bin $m_{c\bar{c}} \in [60, 65]$ GeV is a genuine effect in our calculation. It originates from the NLO contributions associated to $qg \to Q\bar{Q}q$ (and the corresponding collinear counterterm) with purely photon exchange — this term can be considered as part of the QED correction to the LO transition $g\gamma \to Q\bar{Q}$. The scale dependence of the NLO corrections would normally compensate that of the LO contribution, which is however absent in our computation due to the missing photon PDF. This increased scale dependence has a permille effect on the total cross section.

To conclude the discussion of the differential cross sections, we present predictions for b-jet pair production within the LHCb acceptance as a function of the minimum angular separation $\phi_{b\bar{b}}^{\min}$ between the b-jets. In the LHCb analysis [4], a cut $\phi_{b\bar{b}} > 2.6$ is imposed, and said to provide improved sensitivity to the asymmetry of the signal process by enhancing "non-gg production mechanisms". In section 4 we will show that the value of this cut is not so important for the signal process, however it is still likely to be relevant for reducing the background contribution from light-flavoured jets. An experimental study of this distribution may therefore be useful when studying/reducing the contamination of background events. The relevant predictions for pp collisions at $\sqrt{s} = 13$ TeV are presented in figure 4 for the invariant mass bins of $m_{b\bar{b}} \in [75, 105]$ GeV (left) and $m_{b\bar{b}} \in [105, 300]$ GeV (right). The kinematic requirements on the b-jets are indicated in the plots, and are consistent with the standard cuts introduced in (2.2).

3.2 Cross-section ratios

In addition to the measurements of the $b\bar{b}$ and $c\bar{c}$ cross sections discussed in the last section, it is also of interest to perform measurements of the cross-section ratio between the different heavy-quark types. As the theoretical predictions for the cross-section ratios are very precise, these measurements will provide an important experimental benchmark for testing and validating the (charged) flavour-tagging efficiency and mis-tag rates.

JHEP03(2019)166

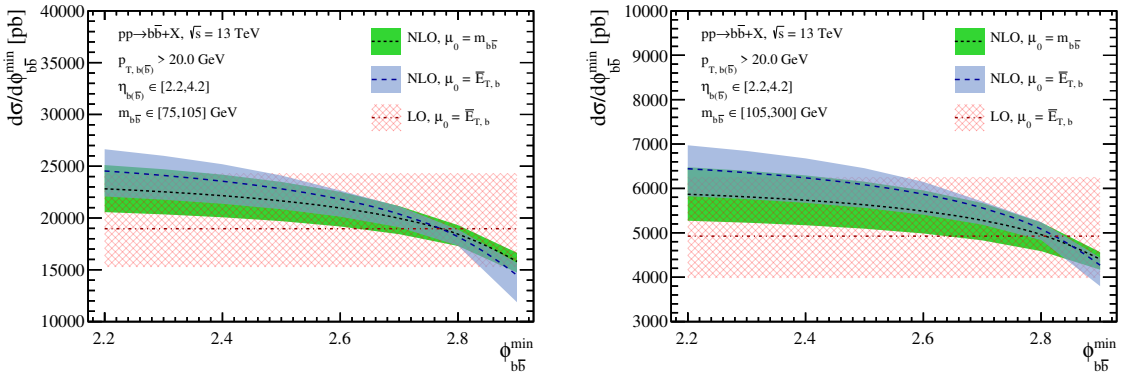

Figure 4. Dependence of the $b\bar{b}$ cross section on the minimum angular separation $\phi^{\min}_{b\bar{b}}$ between the b-jets. The two plots correspond to the invariant-mass regions $m_{b\bar{b}} \in [75, 105]\,\text{GeV}$ (left) and $m_{b\bar{b}} \in [105, 300]\,\text{GeV}$ (right). The NLO results are obtained for $\mu_0 = m_{Q\bar{Q}}$ and $\mu_0 = \overline{E}_{T,Q}$, while the LO distributions employ $\mu_0 = \overline{E}_{T,Q}$ and only shown for comparison.

Our predictions for the cross-section ratio of c- and b-jet pairs at the 13 TeV LHC in the phase-space region (2.2) are shown in figure 5. These distributions are obtained with $\mu_0 = m_{Q\bar{Q}}$, and the uncertainty has been evaluated by correlating the scale variations between the charm- and bottom-quark predictions. In the considered $m_{Q\bar{Q}}$ range, the ratio between the $c\bar{c}$ and $b\bar{b}$ cross sections is below 1. The observed deviation of the ratio from 1 can be attributed to the mass dependence of the LO cross section — see figure 1 (left) — and also to the different EW charges of up- and down-type quarks which affects the ratio both close to and away from the Z peak. In figure 5 (left), the NLO ratio is also displayed for the case that the $\mathcal{O}(\alpha\alpha_s^2)$ corrections have been removed. These corrections arise dominantly in the form of QED corrections to the $gg \to Q\bar{Q}$ subprocess. They are negative and amount to effects of the order of $e_Q^2 \cdot 1\%$ on the spectra, where e_Q denotes the electric charge of the heavy quark Q. While the $\mathcal{O}(\alpha\alpha_s^2)$ contributions thus have a negligible impact at the level of the cross sections, they have a visible effect on the ratio of the symmetric rates.

As discussed in section 2, we have chosen to use PDFs that do not include a photon PDF, and as a result photon-initiated contributions are not included in our computations. To assess the potential uncertainty due to these missing contributions, we have recomputed the ratio of the $c\bar{c}$ and $b\bar{b}$ spectra at LO with the `LUXqed15` PDF set. An uncertainty is then calculated according to

$$\delta R_\gamma = \frac{\sigma(pp \to c\bar{c})}{\sigma(pp \to b\bar{b})} - \left(\frac{\sigma(pp \to c\bar{c})}{\sigma(pp \to b\bar{b})}\right)_{\text{no photon PDF}}, \tag{3.1}$$

where the second ratio is computed excluding all photon-initiated contributions. The modulus of this uncertainty is then added linearly to the scale uncertainty, both in the positive and negative directions. The corresponding results are computed at NLO accuracy with $\mu_0 = m_{Q\bar{Q}}$ and shown in figure 5 (right). Computing the uncertainty this way is likely to overestimate the total theoretical uncertainties. However, to our knowledge, the only publicly available PDF sets based on the precise `LUXqed15` photon PDF determination are NNLO QCD accurate or have been determined at NLO QCD accuracy while fitting

JHEP03(2019)166

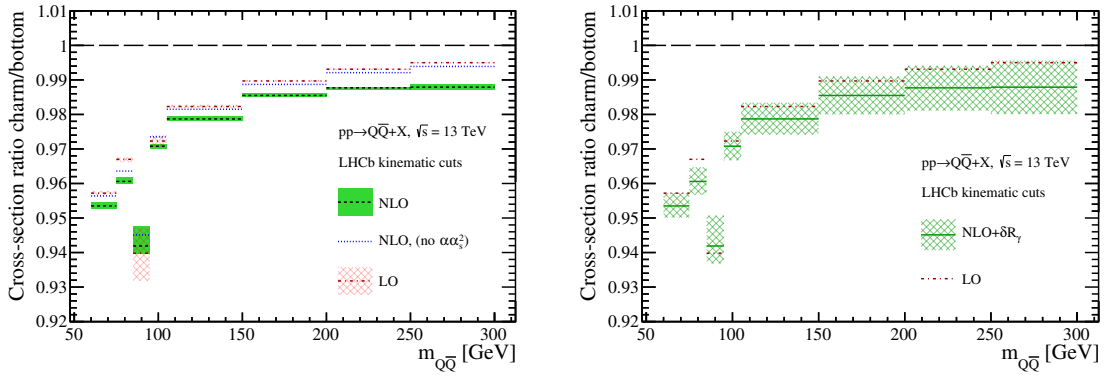

Figure 5. Ratio between the differential cross section of c- and b-jet pair production at the 13 TeV LHC. Left: LO and NLO distributions for $\mu_0 = m_{Q\bar{Q}}$, as well as the NLO distribution obtained without the $\mathcal{O}(\alpha\alpha_s^2)$ corrections. Right: NLO distribution obtained with $\mu_0 = m_{Q\bar{Q}}$, where an additional uncertainty due to photon-induced contributions has been included as explained in the main text. The central value of the LO distribution is also shown for reference.

an intrinsic charm-quark PDF. Using either of these PDF sets for the current predictions would introduce some level of inconsistency. At present, we therefore recommend to use the conservative uncertainty including δR_γ when comparing our results to future data.

4 Asymmetry predictions

In this section we provide differential predictions for the asymmetries as defined in (2.3). These predictions are obtained by separately computing both the numerator and denominator of this expression at NLO, i.e. including terms up to $n + m = 3$ in the expansion defined in (2.1). The corresponding LO results are obtained by including terms up to $n + m = 2$. The exception is that we also take into account the $\mathcal{O}(\alpha_s^3)$ contribution to the numerator when evaluating the asymmetry at LO. This procedure is motivated by the well-known fact that the $\mathcal{O}(\alpha_s^2)$ corrections do not generate an asymmetry in the SM, so that the $\mathcal{O}(\alpha_s^3)$ terms should be considered the leading contribution to the asymmetry. In fact, these terms are numerically dominant except for $m_{Q\bar{Q}}$ values close to the Z pole.

In figure 6 our results for the $b\bar{b}$ (left) and $c\bar{c}$ (right) asymmetries are presented. The NLO predictions corresponding to the two different scales choices (2.5) lead to consistent results across the considered mass range. Close to the Z peak it is found that the NLO corrections have an important impact on the absolute value of the asymmetries as well as the uncertainty estimates. In both the low- and high-mass regions, the uncertainty estimate from the LO prediction is artificially small and should not be considered robust.

Compared to the results presented in [14], our current predictions include the following improvements. First, a jet definition consistent with the LHCb flavour-tagging algorithm [16] is used throughout. Second, based on the recent measurement of $b\bar{b}$ production in the vicinity of the Z peak [17], numerical predictions for both the cross section and asymmetry are provided in fine bins in this invariant-mass region. Third, more precise theoretical predictions are obtained by including a number of subleading NLO corrections, which were

JHEP03(2019)166

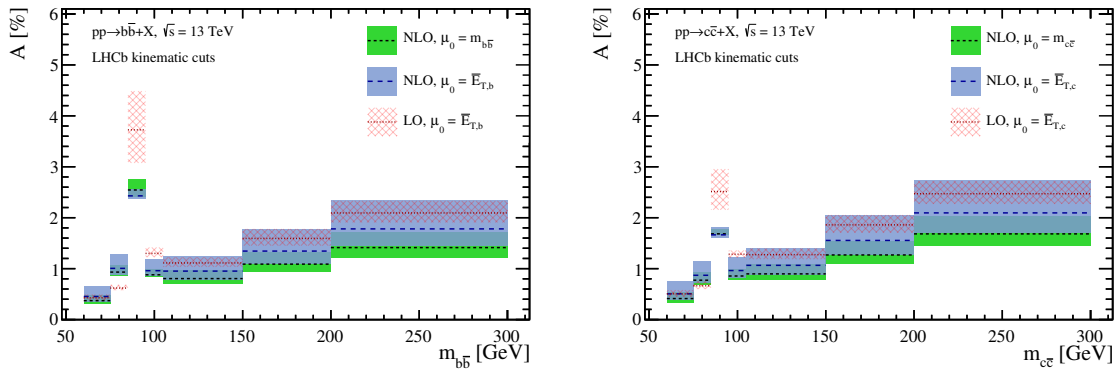

Figure 6. Differential asymmetries for b- (left) and c-jet (right) pairs within the LHCb acceptance (2.2) at $\sqrt{s} = 13\,\text{TeV}$. The NLO (LO) results have been obtained for $\mu_0 = m_{Q\bar{Q}}$ and $\mu_0 = \overline{E}_{T,Q}$ ($\mu_0 = \overline{E}_{T,Q}$), and the shown error bands correspond to scale variations.

previously absent. Fourth, the numerical predictions are computed with updated PDFs which include LHC data, and have been obtained with two reference scale settings which lead to a more reliable uncertainty estimate. These improvements should allow for a more precise comparison to data, which can in turn be used to perform more stringent tests of the SM as well as new physics. Two applications along these lines are discussed in section 5.

Before discussing these applications, it is important to estimate the potential sensitivity of future experimental measurements. The original measurement of the b-jet pair asymmetry at LHCb was performed with an integrated luminosity of $1\,\text{fb}^{-1}$ collected at 7 TeV [4]. Results were presented in the $m_{b\bar{b}}$ bins of $[40, 75]\,\text{GeV}$, $[75, 105]\,\text{GeV}$ and $[105, 300]\,\text{GeV}$, and the measurement was statistically limited in each bin. To estimate the statistical sensitivity expected at 13 TeV, we compute the corresponding uncertainties via

$$\delta A^2_{\text{stat}} = \frac{(1 - A^2)}{N}\,, \tag{4.1}$$

where A denotes the central value of the NLO asymmetry obtained with $\mu_0 = m_{Q\bar{Q}}$, and N is the expected number of events within the data set. To calculate N, we use our cross-section predictions, assume a data set of $5\,\text{fb}^{-1}$, and further apply experimental efficiencies for the reconstruction of a pair of charged- and flavour-tagged jets of $\epsilon_{b\bar{b}} = 0.6\%$ and $\epsilon_{c\bar{c}} = 0.3\%$. The values of these efficiencies are obtained by inverting (4.1) for the 7 TeV measurement [4] using the corresponding central NLO prediction at 7 TeV. We note that the value of $\epsilon_{b\bar{b}} = 0.6\%$ corresponds to a factor of two improvement compared to what has been achieved in the original measurement.

The results of our sensitivity study are shown in figure 7, where the projections for the statistical uncertainties (4.1) are overlaid on the predictions for the b- (left) and c-jet (right) pair asymmetries. This study indicates that a significant improvement in statistical precision will be achievable with future data sets, and that finely binned measurements close to the Z pole should be possible. This is a consequence of the higher cross sections, the increased data sample size, and the assumption about the improved signal efficiency. In the event that a data sample of $50\,\text{fb}^{-1}$ is collected at LHCb [67] (such as in the high-luminosity

JHEP03(2019)166

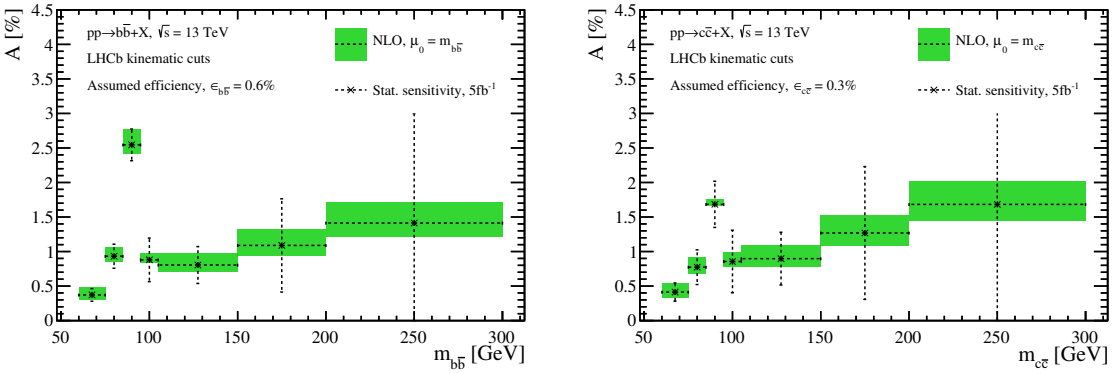

Figure 7. Differential asymmetry for b- (left) and c-jet (right) pairs within the LHCb fiducial region (2.2) at $\sqrt{s} = 13\,\text{TeV}$. The shown NLO distributions are obtained with the scale choice $\mu_0 = m_{Q\bar{Q}}$, and the estimated statistical sensitivity of a future measurement at LHCb with $5\,\text{fb}^{-1}$ of integrated luminosity has been indicated.

phase of the LHC), it is likely that measurements of the heavy-quark asymmetries will be systematically and not statistically limited.

We conclude this section by returning to the choice of the angular cut $\phi_{Q\bar{Q}}$ used in defining the fiducial region (2.2). As mentioned in section 3, the motivation for introducing this cut is to increase the sensitivity to the asymmetry by enhancing "non-gg production mechanisms". To assess this statement, we study the impact of the choice of $\phi^{\text{min}}_{Q\bar{Q}}$ on the observable $\sigma_A/\sigma_S^{1/2}$, where $\sigma_{S\,(A)}$ is the (a)symmetric production cross section. The motivation behind this definition is that the significance of a statistically limited measurement of the asymmetry is approximately $A/\delta A_{\text{stat}}$. Our definition is therefore useful as it estimates the overall statistical sensitivity to the asymmetry measurement itself, rather than just the asymmetry. This is relevant because, while the value of the asymmetry may increase as the value of the cut $\phi^{\text{min}}_{Q\bar{Q}}$ is increased, the number of analysed events simultaneously decreases. Our predictions for $\sigma_A/\sigma_S^{1/2}$ as a function of $\phi^{\text{min}}_{b\bar{b}}$ are shown in figure 8. The two different sets of predictions correspond to the results restricted to the invariant mass bins $m_{b\bar{b}} \in [75, 105]\,\text{GeV}$ and $m_{b\bar{b}} \in [105, 300]\,\text{GeV}$. The obtained distributions are close to flat as $\phi^{\text{min}}_{b\bar{b}}$ increases, indicating that from a statistical point of view the sensitivity to the asymmetry is not improved by requiring larger $\phi^{\text{min}}_{b\bar{b}}$ values. We have therefore chosen to provide predictions for $\phi^{\text{min}}_{Q\bar{Q}} = 2.6$, which matches the original value advocated in [4]. It is worth noting that the choice of this cut may also be important for background rejection (i.e. from light jets). In the far future, if the asymmetry measurements becomes systematically limited, it may be useful to perform a dedicated study of this issue.

5 Applications

In this section we present two applications of our calculations of heavy-quark production. We will first discuss the model-independent constraints that future LHCb measurements of the ratio of the $b\bar{b}$ and $c\bar{c}$ asymmetry may allow to set on the couplings of the Z boson to

JHEP03(2019)166

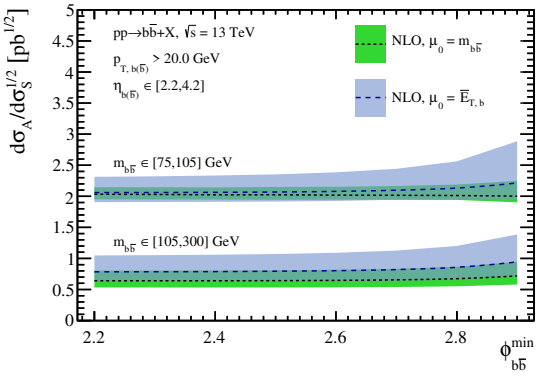

Figure 8. Asymmetric $b\bar{b}$ cross section within $m_{b\bar{b}} \in [75, 105]\,\text{GeV}$ and $m_{b\bar{b}} \in [105, 300]\,\text{GeV}$ normalised to the square root of the symmetric cross section as a function of $\phi^{\text{min}}_{b\bar{b}}$. The shown NLO predictions correspond to the LHCb fiducial region (2.2) at $\sqrt{s} = 13\,\text{TeV}$, and employ the two scale choices introduced in (2.5). The depicted error bands are due to scale variations.

bottom- and charm-quark pairs. We will compare the results of our sensitivity studies to the constraints on the $Zb\bar{b}$ and $Zc\bar{c}$ couplings that arise from the Z-pole measurements performed at LEP [1]. Our second application consists in using the recent LHCb measurement of $Z \to b\bar{b}$ production [17] to put constraints on the new-physics model proposed in [68] which aims at explaining the long-standing LEP anomaly of the forward-backward asymmetry of the bottom quark.

5.1 Constraints on $Zb\bar{b}$ and $Zc\bar{c}$ couplings

Similarly to the top-quark asymmetry, the dominant contribution to the asymmetry of bottom- and charm-quark arises from QCD for most values of the invariant mass of the heavy-quark pair. An important exception is the mass region close to the Z-pole, where the double-resonant contribution from Z-Z interference becomes dominant, and accounts for the bulk of the total asymmetry [12–14]. Measurements of the bottom- and charm-quark asymmetry can therefore be used to set limits on the $Zb\bar{b}$ and $Zc\bar{c}$ couplings [13].

In order to put model-independent constraints on the Z-boson couplings to bottom and charm quarks, we consider in the following the ratio $R_{b/c} = A_b/A_c$ of the asymmetry in $b\bar{b}$ and $c\bar{c}$ production restricted to the mass bin $[75, 105]\,\text{GeV}$. This ratio can be predicted to high accuracy in the SM [14], since many uncertainties cancel between numerator and denominator. For pp collisions at $\sqrt{s} = 13\,\text{TeV}$ and employing the standard LHCb cuts (2.2), we find within the SM the result

$$R^{\text{SM}}_{b/c} = 1.33 \pm 0.07\,. \tag{5.1}$$

The given central value corresponds to the reference scale choice $\mu_0 = m_{Q\bar{Q}}$ and the quoted uncertainty of around 5% includes scale variations as described in section 2.4 and PDF uncertainties. The dominant source of uncertainty arises from missing higher-order QCD corrections, meaning that the stated total uncertainty is in principle improvable by including NNLO corrections. We add that using instead the scale setting $\mu_0 = \overline{E}_{T,Q}$ leads to

JHEP03(2019)166

a central value of $R_{b/c}^{\rm SM}$ that agrees within errors with that in (5.1) and to a comparable total uncertainty. It is worth noting that the above prediction for $R_{b/c}$ corresponds to a specific bin around the Z-boson resonance, and that the prediction is sensitive to the exact location and width of the bin. It will therefore be important to carefully assess the impact of potential bin-to-bin migration effects as part of the experimental measurement of the ratio $R_{b/c}$. Our code can be made available upon request, and can be used to assess the related systematic uncertainty.

The experimental measurements of the EW Z-pole observables obtained at LEP can be used to precisely extract the Z-boson couplings to all SM quarks but the top quark. In the case of the $Zb\bar{b}$ and $Zc\bar{c}$ couplings the combined results are [1]

$$\begin{aligned} g_L^b &= -0.4182 \pm 0.0015\,, \qquad & g_R^b &= 0.0962 \pm 0.0063\,, \\ g_L^c &= 0.3453 \pm 0.0036\,, \qquad & g_R^c &= -0.1580 \pm 0.0051\,, \end{aligned} \tag{5.2}$$

and the corresponding correlation matrix is given by [1]

$$\rho = \begin{pmatrix} 1.00 & 0.88 & -0.09 & -0.17 \\ 0.88 & 1.00 & -0.14 & -0.13 \\ -0.09 & -0.14 & 1.00 & 0.30 \\ -0.17 & -0.13 & 0.30 & 1.00 \end{pmatrix}. \tag{5.3}$$

The SM predictions for the $Zb\bar{b}$ and $Zc\bar{c}$ couplings can be extracted with the help of `ZFITTER` [69] and read

$$\begin{aligned} (g_L^b)^{\rm SM} &= -0.42114\,, \qquad & (g_R^b)^{\rm SM} &= 0.077420\,, \\ (g_L^c)^{\rm SM} &= 0.34674\,, \qquad & (g_R^c)^{\rm SM} &= -0.15470\,. \end{aligned} \tag{5.4}$$

Since the uncertainties associated with (5.4) are negligible compared to the uncertainties quoted in (5.2) only the central values of the SM expectations have been given here. Compared to the experimental measurements (5.2) and (5.3) the SM values (5.4) have a χ^2 per degree of freedom (χ^2/dof) of 2.8.

In figure 9 we show the relative deviations of $R_{b/c}$ in four different planes of $Zb\bar{b}$ and $Zc\bar{c}$ couplings. Overlaid in green are the 68% CL regions that follow from the LEP measurements (5.2) and (5.3). The SM and best-fit points are indicated by black dots and black crosses in the figure. Numerically, we find that the best fits lead to relative deviations of -2.4%, 1.1%, -0.4% and -0.8% in $R_{b/c}$ in the g_L^b–g_R^b (upper left), g_L^c–g_R^c (upper right), g_L^b–g_L^c (lower left) and g_R^b–g_R^c (lower right) plane, respectively. These numbers indicate that for future LHCb measurements of the $b\bar{b}$ and $c\bar{c}$ asymmetries to reach the sensitivity of the existing LEP constraints on the $Zb\bar{b}$ and $Zc\bar{c}$ couplings, determinations of the ratio $R_{b/c}$ at the percent level are needed. Notice that to reach this goal not only the experimental precision but also the theoretical accuracy of the SM predicition (5.1) needs to be improved. Such a theoretical improvement would require the inclusion of NNLO QCD corrections in the prediction of $R_{b/c}$, which is technically viable in view of [43].

JHEP03(2019)166

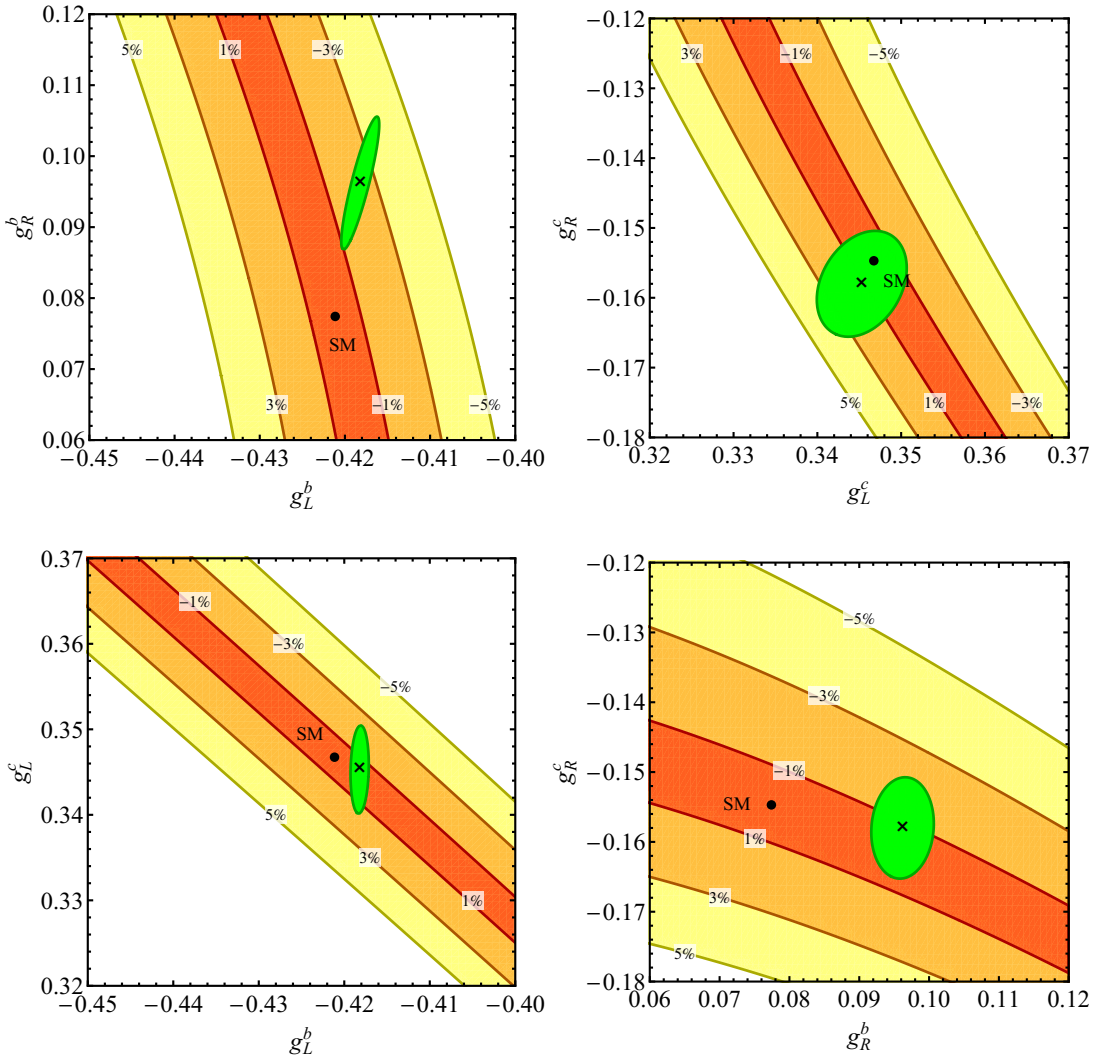

Figure 9. Relative deviations of the ratio $R_{b/c}$ in the g_L^b–g_R^b (upper left), g_L^c–g_R^c (upper right), g_L^b–g_L^c (lower left) and g_R^b–g_R^c (lower right) plane. For comparison also the 68% confidence level (CL) regions favoured by the LEP measurements of the EW Z-pole observables are shown. The SM and best-fit points are indicated by black dots and black crosses, respectively.

5.2 Constraints on new light gauge bosons

Precision measurements of the gauge sector have shown agreement with expected SM properties at the permille level. Among the many observables, the bottom-quark forward-backward asymmetry A_{FB}^b measured at LEP however presents a 3σ deviation with respect to the values expected in the SM [1]. While this deviation could be a result of statistical fluctuations, it is intriguing since it also could be associated with a large modification of the right-handed $Zb\bar{b}$ coupling (cf. (5.2) and (5.4)), which can for instance arise if the Z boson is mixed with additional neutral gauge bosons.

JHEP03(2019)166

A recently proposed model [68] that aims at explaining the long-standing LEP anomaly of $A_{\rm FB}^b$ contains a new $\mathrm{U}(1)_D$ boson (the corresponding mass eigenstate will be called Z' in what follows), which couples with opposite charges to the right-handed components of the bottom and charm quarks. The low-energy spectrum of the model also includes two Higgs doublets, a singlet, and a charged and a neutral vector-like singlet, the latter being a good dark matter candidate. The phenomenology of the Z and the Z' bosons is fully described by the masses M_Z and $M_{Z'}$ of the two gauge bosons, the new coupling constant g_D, the sine s_α of the mixing angle α of the neutral weak eigenstates and the mixings of the bottom (charm) quark with a heavy vector-like bottom (charm) partner, parameterised by the four variables $s_{b,L}$, $s_{b,R}$, $s_{c,L}$ and $s_{c,R}$.

The following values of the $\mathrm{U}(1)_D$ gauge coupling and the mixing parameters

$$g_D = 0.36\,, \quad s_\alpha = -0.03\,, \quad s_{b,L} = -0.07\,, \quad s_{c,L} = -0.1\,, \quad s_{b,R} = s_{c,R} = -0.001\,, \tag{5.5}$$

have been used in the article [68] as a benchmark. In fact, for these choices the $Zb\bar{b}$ and $Zc\bar{c}$ couplings in the $\mathrm{U}(1)_D$ model take the values

$$\begin{aligned} (g_L^b)^{\mathrm{U}(1)_D} &= -0.4185\,, & (g_R^b)^{\mathrm{U}(1)_D} &= 0.0920\,, \\ (g_L^c)^{\mathrm{U}(1)_D} &= 0.3416\,, & (g_R^c)^{\mathrm{U}(1)_D} &= -0.1693\,. \end{aligned} \tag{5.6}$$

These couplings lead to a χ^2/dof of 1.6, which represents a visible improvement compared to the χ^2/dof value quoted after (5.4).

Constraints on the Peskin-Takeuchi parameter T now put a bound on the size of the allowed mass splitting $M_{Z'} - M_Z$ [68]. For the s_α value given in (5.4), one finds that the constraint $T = 0.07 \pm 0.12$ [70] translates into the following 95% CL limit on the mass of the new gauge boson

$$M_{Z'} \in [91.2, 174]\,\mathrm{GeV}\,. \tag{5.7}$$

As pointed out in [68], the presence of a Z' boson in this mass range is subject to several constraints. The first constraint comes from the CMS search [71] for narrow spin-1 resonances decaying to a $q\bar{q}$ pair in association with a high-transverse momentum jet from ISR. Other relevant constraints arise from the $Z' \to \ell^+\ell^-$ searches [72, 73]. For the benchmark parameters (5.5) the combination of the constraints [71–73] can however be shown to be fulfilled for most of the Z'-boson masses in (5.7). In fact, the search [71] features an 2.9σ local excess for dijet invariant masses around 115 GeV, which has been interpreted in [68] as a Z' boson in the $\mathrm{U}(1)_D$ model with $M_{Z'} \simeq 115\,\mathrm{GeV}$ and (5.6).

In the following, we point out that Z' boson with the properties (5.6) and (5.7), can also be probed by the LHCb measurement of $Z \to b\bar{b}$ production in the forward direction [17]. To this purpose, we show in figure 10 four different dijet mass (m_{jj}) distributions predicted in the $\mathrm{U}(1)_D$ model (blue curves). The chosen parameters are given in (5.5). The background-subtracted dijet mass distribution[6] as measured by the LHCb collaboration in [17] (black error bars), the SM prediction (red curves) and the one standard deviation total uncertainty band (grey bands) is also displayed. From the upper left panel (lower

[6]We thank Lorenzo Sestini for providing the LHCb $Z \to b\bar{b}$ mass model to us.

JHEP03(2019)166

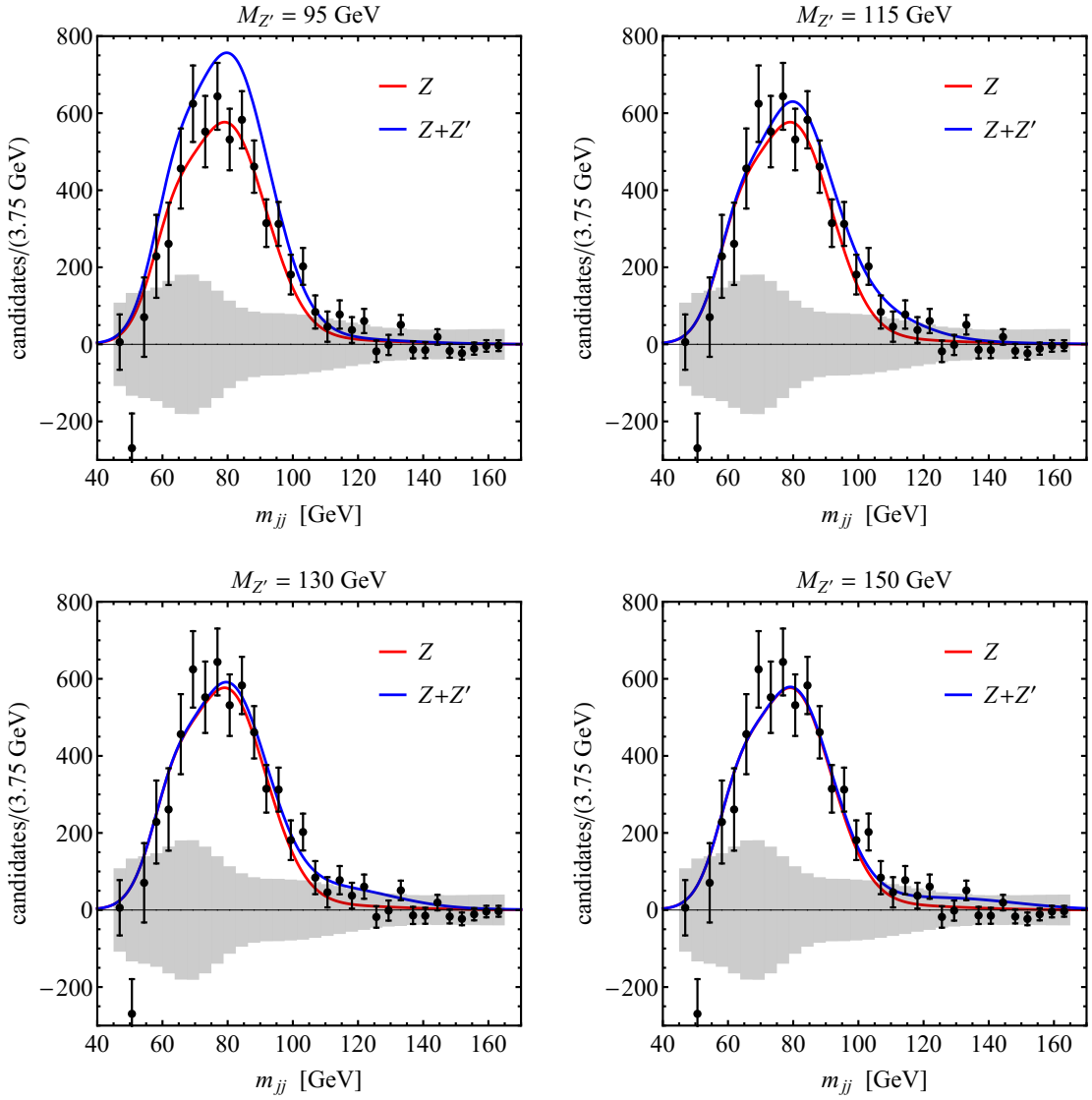

Figure 10. Dijet mass distributions in $Z \to b\bar{b}$ predicted in the $\mathrm{U}(1)_D$ model for different Z' masses (blue curves). All predictions employ the benchmark parameters (5.6). The background-subtracted dijet mass distribution as measured by LHCb in [17] (black error bars), the $Z \to b\bar{b}$ mass model within the SM (red curves) and the one standard deviation total uncertainty band (grey bands) is also shown. The uncertainty band includes statistical and systematic uncertainties. See text for further details.

right panel) one observes that a Z' boson with mass $M'_Z = 95\,\mathrm{GeV}$ ($M'_Z = 150\,\mathrm{GeV}$) is disfavoured by the data since it leads to an excess in the peak region (the tail) of the m_{jj} distribution. This statement is quantified in figure 11 which shows the $\Delta\chi^2$ in the $\mathrm{U}(1)_D$ model as a function of $M_{Z'}$. One sees that for the parameters (5.6) only Z' bosons with masses in the range

$$M_{Z'} \in [108, 135]\,\mathrm{GeV}\,, \tag{5.8}$$

are compatible with the LHCb measurements of $Z \to b\bar{b}$ production at the 95% CL. In fact, the minimum of $\Delta\chi^2$ is located at $M_{Z'} \simeq 120\,\mathrm{GeV}$ in close proximity to the local excess in

JHEP03(2019)166

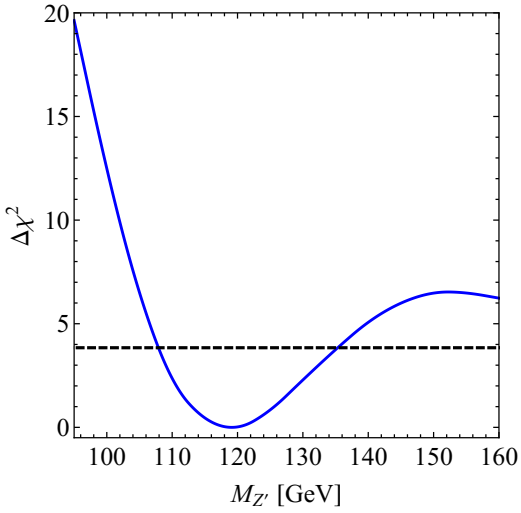

Figure 11. $\Delta\chi^2$ distribution in the $\mathrm{U}(1)_D$ model as a function of the Z'-boson mass following from the LHCb measurement [17]. The benchmark parameters (5.6) have been used to obtain the shown predictions. The dashed black line corresponds to $\Delta\chi^2 = 3.84$, i.e. the 95% CL for a Gaussian distribution.

the CMS measurement [71] observed for dijet masses around 115 GeV. The corresponding χ^2/dof is 1.9 and thus slightly better than the SM fit which leads to $\chi^2/\mathrm{dof} = 2.0$. While the finding that both the CMS and LHCb measurement may indicate that a light new gauge boson is hiding in the data is probably accidental, we emphasise that the two-sided bound (5.8) on the mass of the Z' boson is stronger than the limit that derives from a combination of the searches [71–73].

The above applications of our SM results presented in sections 3 and 4 show that the LHCb experiment can provide unique probes of new physics in heavy-quark production due to its efficient triggering, excellent vertexing and accurate event reconstruction. While already a handful of similar proposals of such "exotic" new-physics searches exist that specifically exploit the remarkable capabilities of LHCb (see e.g. [6, 13, 67, 74–80]), we believe that further research in this rich and developing field can turn out to be potentially very rewarding.

Acknowledgments

We thank Valentin Hirschi, Alexander Huss, Mitesh Patel and Lorenzo Sestini for useful communications and discussions. RG acknowledges support by the Dutch Organization for Scientific Research (NWO) through a VENI grant. UH acknowledges the hospitality and support of the Particle Theory Group at the University of Oxford and the CERN Theoretical Physics Department at various stages of this project. We acknowledge the computing resources provided to us by the Swiss National Supercomputing Centre (CSCS) under the project ID p501b.

JHEP03(2019)166

A Analytic results

In this appendix, we provide predictions for the hadronic process $pp \to Q\bar{Q}X$ assuming the factorisation theorem of the form

$$\mathrm{d}\sigma\left(pp \to Q\bar{Q}X\right) = \sum_{i,j} \int \mathrm{d}x_1\, \mathrm{d}x_2\, f_{i/p}(x_1, \mu_F^2)\, f_{j/p}(x_2, \mu_F^2)\, \mathrm{d}\hat{\sigma}_{ij}\,, \tag{A.1}$$

where the universal PDFs $f_{i/p}(x, \mu_F)$ describe the probability of finding the parton i in the proton with longitudinal momentum fraction x and μ_F is the factorisation scale. In analogy to (2.1), the differential partonic cross sections $\mathrm{d}\hat{\sigma}_{ij}$ may be written as an expansion in terms of the electromagnetic and strong coupling constant according to

$$\mathrm{d}\hat{\sigma}_{ij} = \sum_{n,m} \alpha^n \alpha_s^m\, \mathrm{d}\hat{\sigma}_{ij}^{(n,m)}\,, \tag{A.2}$$

where $\mathrm{d}\hat{\sigma}_{ij}^{(n,m)}$ denotes the differential partonic cross sections for the initial state ij with the α and α_s factors stripped off.

The differential cross sections can be further decomposed to isolate the contributions which are asymmetric under interchange of the final state heavy quark and antiquark according to

$$\mathrm{d}\hat{\sigma}_{ij,A} = \frac{1}{2}\left[\mathrm{d}\hat{\sigma}\left(ij \to Q\bar{Q}X\right) - \mathrm{d}\hat{\sigma}\left(ij \to \bar{Q}QX\right)\right]. \tag{A.3}$$

Here the notation indicates that in the process labelled by $ij \to Q\bar{Q}X$ ($ij \to \bar{Q}QX$) the angle θ corresponds to the scattering angle of the heavy quark (heavy antiquark) in the partonic centre-of-mass (CM) frame. The benefit of this decomposition is that the symmetric and asymmetric contributions to the cross sections can be numerically integrated separately, which substantially improves the efficiency of the numerical evaluation.

The results in this work have been obtained at NLO accuracy ($n + m = 3$) for both symmetric and asymmetric contributions. Relevant results for the differential cross sections to this accuracy have previously been obtained in [20–29, 81], and in many cases the analytic results have been given. The purpose of this appendix is to collect the analytic results for asymmetric bottom- and charm-quark pair production, suitable for direct numerical integration. We will provide analytic expressions for both the (renormalised) virtual and real emission contributions to the partonic cross section for various subprocesses, which contain explicit and implicit divergences, respectively. A number of these contributions contain only soft divergences, and so we have also included a soft function which describes the radiation of soft gluons integrated in phase space up to a cut E_{cut} in the gluon energy. This function is suitable for applying the technique of phase-space slicing [41], which is found to be stable for these types of processes. In cases where both soft and collinear divergences are present, we have also regularised the numerical integration using dipole subtraction [42]. In the next subsection, we introduce our notation for describing the kinematics of two- and three-body partonic final states, and then list the relevant formulas ordered by their powers in the expansion (A.2).

JHEP03(2019)166

A.1 Kinematics and notation

The partonic cross section for heavy-quark pair-production receives Born-level contributions from gluon fusion, quark annihilation as well as gluon-photon and photon-photon scattering. As an example of a partonic $2 \to 2$ subprocess, we consider quark annihilation

$$q(p_1) + \bar{q}(p_2) \to Q(p_3) + \bar{Q}(p_4)\,, \tag{A.4}$$

where the four-momenta $p_{1,2}$ of the initial-state partons can be expressed as the fractions $x_{1,2}$ of the four-momenta $P_{1,2}$ of the colliding protons. The partonic cross section is a function of the kinematic invariants

$$\hat{s} = (p_1 + p_2)^2\,, \qquad \hat{t}_Q = (p_1 - p_3)^2 - m_Q^2\,, \qquad \hat{u}_Q = (p_2 - p_3)^2 - m_Q^2\,, \tag{A.5}$$

and momentum conservation implies that $\hat{s} + \hat{t}_Q + \hat{u}_Q = 0$. In addition to $\hat{s}$, $\hat{t}_Q$ and $\hat{u}_Q$, we also use the velocity of the heavy quark and scattering angle

$$\beta = \sqrt{1 - \frac{4m_Q^2}{\hat{s}}}\,, \qquad c = \beta \cos\theta\,, \tag{A.6}$$

to write our results, where θ denotes the angle between $\vec{p}_1$ and $\vec{p}_3$ in the partonic CM frame. Notice that

$$\hat{t}_Q = -\frac{\hat{s}}{2}\,(1 - c)\,, \qquad \hat{u}_Q = -\frac{\hat{s}}{2}\,(1 + c)\,, \tag{A.7}$$

which implies that $c = (\hat{t}_Q - \hat{u}_Q)/\hat{s}$, and as a result the variable c is strictly speaking not needed when writing our results. In some cases we will however use c, because the obtained expressions turn out to be more compact than those written in terms of $\hat{s}$, $\hat{t}_Q$ and $\hat{u}_Q$. In addition to these kinematic variables, it also useful to introduce the following mass variables

$$y_Q = \frac{m_Q^2}{\hat{s}}\,, \qquad y_W = \frac{M_W^2}{\hat{s}}\,, \qquad \mu_Z = M_Z^2 - i\Gamma_Z M_Z\,. \tag{A.8}$$

The complex squared-mass μ_Z is introduced as the Z boson is treated as an unstable particle throughout our calculation. This is necessary when describing bottom- and charm-quark pair production in the vicinity of the Z-boson resonance.

The NLO corrections also involves the evaluation of $2 \to 3$ real emission processes of the form

$$q(p_1) + \bar{q}(p_2) \to Q(p_3) + \bar{Q}(p_4) + g(p_5)\,, \tag{A.9}$$

where again we have used the quark-annihilation subprocess as an example. The analytic formula for these processes are provided in terms of the following dimensionless variables

$$y_{ij} = \frac{2\,p_i \cdot p_j}{\hat{s}}\,. \tag{A.10}$$

All $2 \to 3$ processes can be characterised by five independent scalar quantities [22]. For instance, choosing y_{14}, y_{23}, y_{34}, y_{35} and y_{45}, the remaining five y_{ij} variables are related (by

JHEP03(2019)166

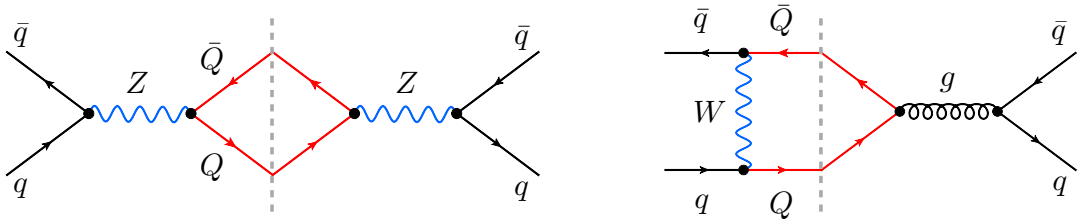

Figure 12. Left: tree-level s-channel Z-boson exchange contribution to asymmetric heavy-quark production at $\mathcal{O}(\alpha^2)$. Right: interference contribution between t-channel W-boson exchange and tree-level s-channel gluon exchange. In both diagrams the relevant particle cuts are represented by a dashed line. See text for further details.

momentum conservation) to the made choices by the following equalities

$$\begin{aligned} y_{14} &= y_{12} - y_{13} - y_{15}\,, \\ y_{23} &= y_{12} - y_{24} - y_{25}\,, \\ y_{34} &= y_{12} - y_{15} - y_{25} - 2y_Q\,, \\ y_{35} &= y_{13} + y_{15} - y_{24}\,, \\ y_{45} &= -y_{13} + y_{24} + y_{25}\,. \end{aligned} \tag{A.11}$$

We emphasise that below we will write the $2 \to 3$ results such that the obtained expressions become as short as possible, and as a result our formulas will involve more than five independent y_{ij} parameters.

A.2 $\mathcal{O}(\alpha^2)$ contributions

The asymmetric $\mathcal{O}(\alpha^2)$ effects arise from the interference between the partonic processes $q\bar{q} \to Z/\gamma \to Q\bar{Q}$. The relevant diagram with s-channel Z-boson exchange is shown on the left-hand side in figure 12. In agreement with [82], we obtain for the corresponding asymmetric differential cross section the following compact expression

$$\left(\frac{\mathrm{d}\sigma_{q\bar{q},A}}{\mathrm{d}\cos\theta}\right)_{\mathcal{O}(\alpha^2)} = \frac{\pi\alpha^2}{4}\,\beta c\,\frac{a_q a_Q}{(\hat{s}-M_Z^2)^2+\Gamma_Z^2 M_Z^2}\left[v_q v_Q\,\hat{s} + 2e_q e_Q\left(\hat{s}-M_Z^2\right)\right]. \tag{A.12}$$

where

$$a_f = \frac{T_3^f}{s_w c_w}\,, \qquad v_f = \frac{T_3^f - 2e_f s_w^2}{s_w c_w}\,, \tag{A.13}$$

are the axial-vector and vector coupling of the Z boson to a fermion f. These couplings depend on the third component $T_3^f = \pm 1/2$ of the weak isospin, the electric charge e_f, and the sine s_w and cosine c_w of the weak mixing angle.

A.3 $\mathcal{O}(\alpha\alpha_s)$ contributions

In order to obtain the $\mathcal{O}(\alpha\alpha_s)$ contributions one has to consider interference contributions between t-channel W-boson (and would-be Goldstone boson) exchange and s-channel gluon

JHEP03(2019)166

exchange. A diagram of this kind is given on the right in figure 12. In the case of $c\bar{c}$ production from a $d\bar{d}$ initial state, we arrive at

$$\left(\frac{\mathrm{d}\sigma_{d\bar{d},A}}{\mathrm{d}\cos\theta}\right)_{\mathcal{O}(\alpha\alpha_s)} = \frac{\pi\alpha\alpha_s|V_{cd}|^2}{18s_w^2}\frac{\beta c}{\hat{s}} \times \frac{8y_c^2 + y_c\left(c^2 - 4y_W - 1\right) + 2y_W\left(c^2 + 4y_W + 3\right)}{y_W\left(c^2 - (1 - 2y_c + 2y_W)^2\right)}, \tag{A.14}$$

where V_{cd} denotes the relevant CKM matrix element. Our result (A.14) agrees with the expression given in [13]. In the case of asymmetric $b\bar{b}$ production, the W-boson mediated t-channel contributions are strongly suppressed either by the small CKM element V_{ub} or by a bottom-quark PDF. Consequently, we include (A.14) in our numerical analysis only in the case of charm-quark pair production. As these corrections are numerically small, we have included neither the QCD nor the QED/weak correction to this process in our predictions.

A.4 $\mathcal{O}(\alpha_s^3)$ contributions

There is no asymmetric contribution to the production of heavy-quark pairs at $\mathcal{O}(\alpha_s^2)$. Starting at $\mathcal{O}(\alpha_s^3)$, however, quark annihilation $q\bar{q} \to Q\bar{Q}(g)$ as well as flavour excitation $qg \to Q\bar{Q}q$ receive charge-asymmetric contributions. The gluon-fusion $gg \to Q\bar{Q}X$ subprocess must be convoluted with a symmetric initial state to provide a hadronic cross-section prediction, and so does not lead to an observable asymmetry.

Charge conjugation invariance can be invoked to show that, as far as the virtual corrections to $q\bar{q} \to Q\bar{Q}$ are concerned, only the interference between the lowest-order and the QCD box graphs contributes to the asymmetry at $\mathcal{O}(\alpha_s^3)$. An example of a Feynman diagram that furnishes a contribution is shown on the left-hand side in the upper row of figure 13. The corresponding virtual corrections can be written as

$$\left(\frac{\mathrm{d}\sigma_{q\bar{q},A}}{\mathrm{d}\cos\theta}\right)^{\mathrm{virt}}_{\mathcal{O}(\alpha_s^3)} = \frac{\alpha_s^3 d_{abc}^2}{16N_c^2}\frac{\beta}{\hat{s}}\frac{A(\hat{t}_Q,\hat{u}_Q) - A(\hat{u}_Q,\hat{t}_Q)}{\hat{s}}, \tag{A.15}$$

with $N_c = 3$ and $d_{abc}^2 = 40/3$ colour factors. Here $d_{abc} = 2\,\mathrm{Tr}\left(\left\{T^a, T^b\right\}T^c\right)$, while T^a are the colour generators normalised such that $\mathrm{Tr}\left(T^aT^b\right) = \delta_{ab}/2$. The one-loop function appearing in (A.15) is given by

$$\begin{aligned} A(v,w) = \frac{v}{1-4y_Q}\Bigg[& B_0(\hat{s},0,0) - 4y_Q\left(2 + \frac{v^2 + w^2 - 4\hat{s}^2 y_Q}{2vw}\right)B_0(m_Q^2,0,m_Q^2) \\ & - \hat{s}\,(1-4y_Q)\,C_0(\hat{s},0,0,0,0,0) \\ & - \hat{s}\left(1 - 8y_Q\,(1-y_Q)\right)C_0(\hat{s},m_Q^2,m_Q^2,0,0,m_Q^2)\Bigg] \\ & + \left(w - \frac{2\hat{s}^2 y_Q}{v}\right)B_0(v+m_Q^2,0,m_Q^2) \\ & - v\,(v - w + 2\hat{s}y_Q)\,C_0(0,m_Q^2,x+m_Q^2,0,0,m_Q^2) \\ & - \frac{v}{2}\left(3v^2 + w^2 + 2\hat{s}^2 y_Q\right)D_0(0,0,m_Q^2,m_Q^2,\hat{s},v+m_Q^2,0,0,0,m_Q^2), \end{aligned} \tag{A.16}$$

JHEP03(2019)166

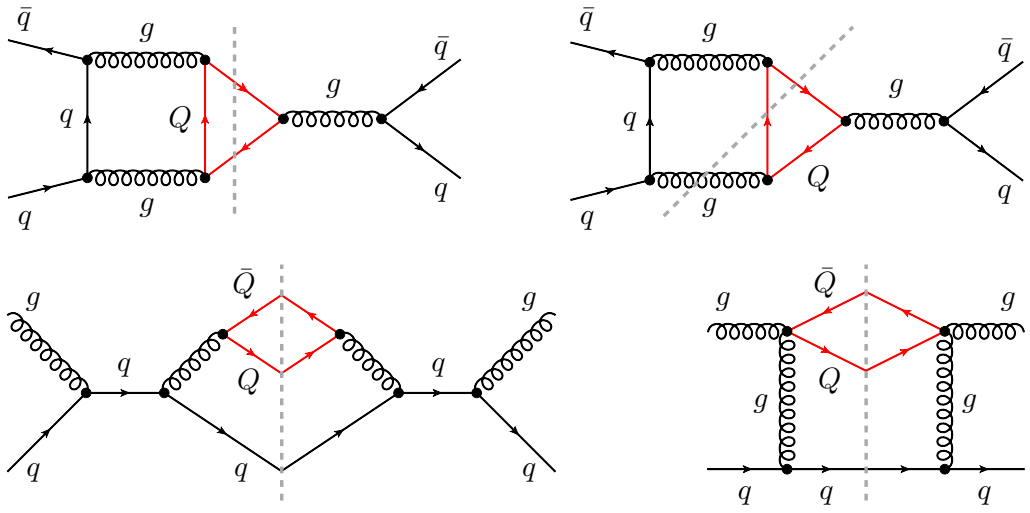

Figure 13. Representative Feynman diagrams that contribute to the asymmetric production cross section of heavy-quark pairs at $\mathcal{O}(\alpha_s^3)$. Upper row: the two-particle cut (right) describes the interference of the one-loop box diagram with the tree-level graph, while the three-particle cut (left) corresponds to the interference of final-state with initial-state gluon corrections. Lower row: three-particle cuts that represent a production of heavy quarks via flavour excitation.

where our definition of the Passarino-Veltman scalar integrals B_0, C_0 and D_0 follows that used in `FormCalc`. We have verified that the formulas (A.15) and (A.16) recover the analytic results given in [83].

As in the case of the virtual contributions also for the real corrections, only the interference between the amplitudes that are odd under the exchange of Q and $\bar{Q}$ leads to a non-zero correction of the form (A.3). A relevant Feynman graph is displayed on the right in the upper row of figure 13. For the real gluon corrections to the asymmetric cross section, we find the result

$$\begin{aligned}\left(\frac{\mathrm{d}\sigma_{q\bar{q},A}}{\mathrm{d}y_{35}\,\mathrm{d}y_{45}\,\mathrm{d}\Omega}\right)^{\text{real}}_{\mathcal{O}(\alpha_s^3)} &= \frac{\alpha_s^3 d_{abc}^2}{64\pi N_c^2}\,\frac{1}{\hat{s}\,y_{12}\,y_{35}\,(y_{34}+2y_Q)} \\ &\times\left\{\frac{y_{13}}{y_{15}}\left[y_{13}^2+y_{14}^2+y_{23}^2+y_{24}^2+2\,(y_{12}+y_{34}+2y_Q)\,y_Q\right]+4y_{24}\,y_Q\right\} \\ &-(1\leftrightarrow 2)-(3\leftrightarrow 4)+(1\leftrightarrow 2,3\leftrightarrow 4)\,,\end{aligned} \tag{A.17}$$

where $d\Omega = d\cos\theta\, d\varphi$ is the differential solid angle with φ the azimuthal angle. The expression given in (A.17) agrees with the results provided in [83].

Soft gluon radiation in the process $q\bar{q}\to Q\bar{Q}g$ integrated in phase space up to a cut E_{cut} in the gluon energy leads to the expression

$$\left(\frac{\mathrm{d}\sigma_{q\bar{q},A}}{\mathrm{d}\cos\theta}\right)^{\text{soft}}_{\mathcal{O}(\alpha_s^3)} = \frac{\alpha_s^3 d_{abc}^2}{32N_c^2}\,\frac{\beta}{\hat{s}}\,S\,, \tag{A.18}$$

JHEP03(2019)166

where

$$S = \left(c^2 + 1 + 4y_Q\right) \left\{ \ln\left(\frac{\hat{t}_Q}{\hat{u}_Q}\right) \left[-\frac{2}{\epsilon} + 2\ln B + 4\ln\left(\frac{E_{\text{cut}}}{\mu}\right)\right] + A(\hat{t}_Q) - A(\hat{u}_Q) \right\}, \quad \text{(A.19)}$$

is the relevant soft function. Here $\epsilon = (4-d)/2$ arises from dimensional regularisation in d dimensions, μ denotes the corresponding renormalisation scale, and we have furthermore introduced

$$A(v) = \ln^2\left(\frac{-v}{\hat{s}\sqrt{y_Q}}\right) + 2\text{Li}_2\left(1 - \frac{Bv}{\hat{s}\sqrt{y_Q}}\right) - 2\text{Li}_2\left(1 - \frac{B\hat{s}\sqrt{y_Q}}{v}\right), \quad B = \sqrt{\frac{1+\beta}{1-\beta}}, \quad \text{(A.20)}$$

with $\text{Li}_2(z) = \int_z^0 dt\, \ln(1-t)/t$ denoting the usual dilogarithm. Our results (A.18), (A.19) and (A.20) can be shown to agree with the expressions presented in [83]. Note that the IR $1/\epsilon$ pole in (A.19) cancels against that in the virtual corrections (A.15) so that the sum of the virtual and soft contributions is IR finite and can be numerically integrated in four dimensions.

The asymmetric $\mathcal{O}(\alpha_s^3)$ contribution to the heavy-quark production cross section that is associated to the flavour excitation process can be obtained from the result (A.17) by crossing, i.e. interchanging the indices $2 \leftrightarrow 5$ in the variables y_{ij} as defined in (A.10). Examples of relevant Feynman diagrams are given in the lower row of figure 13. Noting a difference in the colour factor for averaging over the initial-state gluon with respect to [83], we find the expression

$$\begin{aligned}\left(\frac{\mathrm{d}\sigma_{qg,A}}{\mathrm{d}y_{35}\,\mathrm{d}y_{45}\,\mathrm{d}\Omega}\right)_{\mathcal{O}(\alpha_s^3)} &= \frac{\alpha_s^3 d_{abc}^2}{64\pi N_c\left(N_c^2-1\right)} \frac{1}{\hat{s}\, y_{15}\, y_{23}\left(y_{34}+2y_Q\right)} \\ &\times \left\{ \left(\frac{y_{13}}{y_{12}} - \frac{y_{35}}{y_{25}}\right) \left[y_{13}^2 + y_{14}^2 + y_{35}^2 + y_{45}^2 + 2\left(y_{34} - y_{15} + 2y_Q\right) y_Q\right] \right. \\ &\left. + 4\left(y_{14} + y_{45}\right) y_Q \right\} - (3 \leftrightarrow 4)\,. \end{aligned} \quad \text{(A.21)}$$

The same result also holds in the case of the partonic reaction $\bar{q}g \to Q\bar{Q}\bar{q}$. In contrast to the asymmetric contribution from $q\bar{q} \to Q\bar{Q}g$, the flavour excitation processes $qg \to Q\bar{Q}q$ and $\bar{q}g \to Q\bar{Q}\bar{q}$ are IR finite.

A.5 $\mathcal{O}(\alpha\alpha_s^2)$ contributions

The structure of the $\mathcal{O}(\alpha\alpha_s^2)$ contributions to the asymmetric production cross section of heavy-quark pairs that involve a photon is very similar to that of the pure QCD corrections. In fact, all subprocesses that contribute at $\mathcal{O}(\alpha\alpha_s^2)$ can be obtained from the $\mathcal{O}(\alpha_s^3)$ corrections presented in appendix A.4 by rescaling with

$$R^{\gamma}_{\mathcal{O}(\alpha\alpha_s^2)} = \frac{12\alpha\, e_q\, e_Q}{5\alpha_s}\,. \quad \text{(A.22)}$$

JHEP03(2019)166

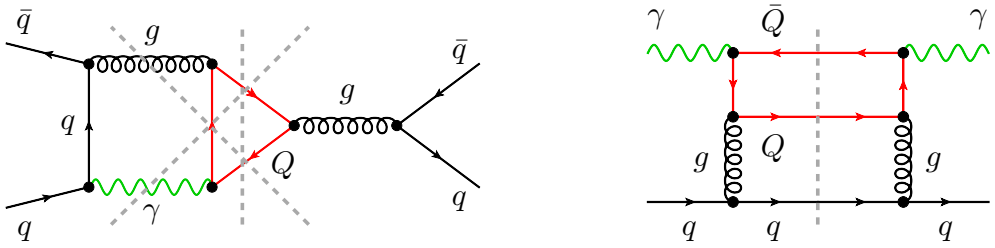

Figure 14. Left: possible two- and three-particle cuts that contribute via $q\bar{q} \to Q\bar{Q}$, $q\bar{q} \to Q\bar{Q}g$ and $q\bar{q} \to Q\bar{Q}\gamma$ to the asymmetric cross section in heavy-quark production at $\mathcal{O}(\alpha\alpha_s^2)$. Right: example of a Feynman diagram that leads to a photon-initiated production asymmetry of heavy quarks at $\mathcal{O}(\alpha\alpha_s^2)$.

Here the factor 12/5 arises from the ratio of QED and QCD colour factors $(N_c^2-1)/4 = 2$ and $d_{abc}^2/16 = 5/6$.

In the case of quark annihilation, we find the following relation between the corrections of $\mathcal{O}(\alpha\alpha_s^2)$ and $\mathcal{O}(\alpha_s^3)$ to the differential asymmetric cross sections

$$(\mathrm{d}\sigma_{q\bar{q},A})^{\gamma}_{\mathcal{O}(\alpha\alpha_s^2)} = 3R^{\gamma}_{\mathcal{O}(\alpha\alpha_s^2)}\,(\mathrm{d}\sigma_{q\bar{q},A})_{\mathcal{O}(\alpha_s^3)}\,, \tag{A.23}$$

irrespectively of whether the contributions are virtual, real or soft. The additional overall factor of 3 reflects the three possible attachments of the photon in diagrams like the one shown on the left-hand side in figure 14. In the case of the qg-initiated transition only two different photon attachments are possible so that

$$(\mathrm{d}\sigma_{qg,A})^{\gamma}_{\mathcal{O}(\alpha\alpha_s^2)} = 2R^{\gamma}_{\mathcal{O}(\alpha\alpha_s^2)}\,(\mathrm{d}\sigma_{qg,A})_{\mathcal{O}(\alpha_s^3)}\,, \tag{A.24}$$

and similarly for $\bar{q}g \to Q\bar{Q}\bar{q}$. Our formulas (A.23) and (A.24) agree with the findings of the article [83]. Finally, in the case of the photon-initiated process $q\gamma \to Q\bar{Q}q$, which receives contributions from Feynman diagrams such as the one displayed on the right in figure 14, we obtain

$$(\mathrm{d}\sigma_{q\gamma,A})^{\gamma}_{\mathcal{O}(\alpha\alpha_s^2)} = 8R^{\gamma}_{\mathcal{O}(\alpha\alpha_s^2)}\,(\mathrm{d}\sigma_{qg,A})_{\mathcal{O}(\alpha_s^3)}\,, \tag{A.25}$$

and the same result applies to the $\bar{q}\gamma$ initial state. Notice that the factor of $N_c^2 - 1 = 8$ arises from averaging over the photon in the initial state rather than the gluon.

As in the case of pure QCD, the $\mathcal{O}(\alpha\alpha_s^2)$ corrections associated to Z-boson exchange receive contributions from both virtual and real corrections. For the interference contributions of box diagrams with tree-level s-channel exchange graphs, we obtain the following expression

$$\begin{aligned}\left(\frac{\mathrm{d}\sigma_{q\bar{q},A}}{\mathrm{d}\cos\theta}\right)^{\mathrm{virt},Z}_{\mathcal{O}(\alpha\alpha_s^2)} = \frac{\alpha\alpha_s^2}{2N_c^2}\,\frac{\beta}{\hat{s}}\,\mathrm{Re}\Bigg\{\left(\frac{v_q v_Q}{\hat{s}-\mu_Z}\right)^{*}\,\big(A(\hat{t}_Q,\hat{u}_Q) - A(\hat{u}_Q,\hat{t}_Q)\big) \\ + \frac{v_q v_Q}{\hat{s}}\,\big(B(\hat{t}_Q,\hat{u}_Q) - B(\hat{u}_Q,\hat{t}_Q)\big)\Bigg\}\,,\end{aligned} \tag{A.26}$$

for the asymmetric heavy-quark pair production cross section. The loop function $A(v,w)$ has already been given in (A.16). It arises in the context of (A.26) from two-particle cut

JHEP03(2019)166

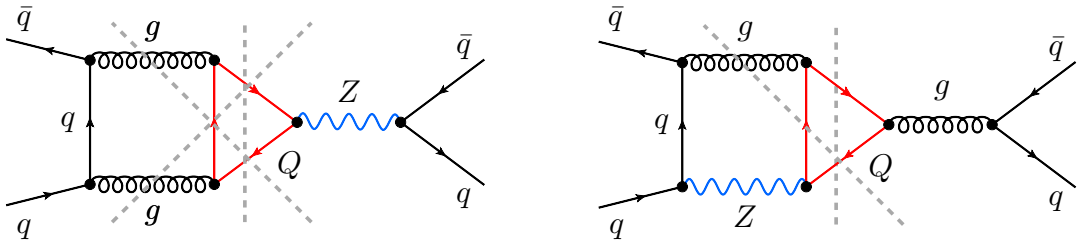

Figure 15. Examples of graphs that affect the production asymmetry of heavy quarks at $\mathcal{O}(\alpha\alpha_s^2)$ and involve the exchange of a Z boson. Consult the main text for additional explanations.

diagrams like the one depicted on the left in figure 15. The function $B(v,w)$ is instead related to two-particle cuts in graphs of the type shown on the right-hand side of the same figure. In terms of standard Passarino-Veltman scalar integrals B_0, C_0 and D_0, we arrive at the result

$$
\begin{aligned}
B(v,w) = \frac{v}{1-4y_Q}\Bigg[& 2B_0(\hat{s},0,\mu_Z) - 2\hat{s}\,(1-4y_Q)\,C_0(\hat{s},0,0,0,0,\mu_Z) \\
& - 4y_Q\left(2+\frac{v^2+w^2-4\hat{s}^2y_Q}{2vw}\right)\Big[B_0(m_Q^2,0,m_Q^2)+B_0(m_Q^2,\mu_Z,m_Q^2)\Big] \\
& - \hat{s}\left(2-16y_Q\,(1-y_Q)-\frac{4\mu_Z\,y_Q}{v+w}\right)C_0(m_Q^2,m_Q^2,\hat{s},0,m_Q^2,\mu_Z)\Bigg] \\
& + 2\left(w-\frac{2\hat{s}^2y_Q}{v}\right)B_0(v+m_Q^2,0,m_Q^2) \\
& - v\left(v-w+2\hat{s}y_Q+\mu_Z\right)C_0(0,m_Q^2,v+m_Q^2,0,0,m_Q^2) \\
& - v\left[v-w+2\hat{s}y_Q+\mu_Z\left(1+\frac{2\hat{s}^2y_Q}{v^2}\right)\right]C_0(v+m_Q^2,m_Q^2,0,0,m_Q^2,\mu_Z) \\
& - v\left(3v^2+w^2+2\hat{s}^2y_Q+2\mu_Z\left(v\,(1-y_Q)-wy_Q\right)+\mu_Z^2\right) \\
& \times D_0(0,m_Q^2,m_Q^2,0,v+m_Q^2,\hat{s},0,0,m_Q^2,\mu_Z)\,.
\end{aligned}
\tag{A.27}
$$

Notice that the these expressions are a function of the complex squared-mass μ_Z, which is necessary to account for the width effects in region close to the Z-boson resonance (this is not required in the case of top-quark pair production since $2m_t > m_Z$). If the calculation is performed in the complex-mass scheme, the couplings v_f become complex as discussed for instance in [60].

The real emission and soft contributions of $\mathcal{O}(\alpha\alpha_s^2)$ can again be obtained by rescaling the corresponding QCD results. We define

$$
R^Z_{\mathcal{O}(\alpha\alpha_s^2)} = \frac{12\alpha\,v_q v_Q}{5\alpha_s}\,. \tag{A.28}
$$

JHEP03(2019)166

In terms of (A.17) and (A.28), we find for the real corrections

$$\left(\mathrm{d}\sigma_{q\bar{q},A}\right)^{\mathrm{real},Z}_{\mathcal{O}(\alpha\alpha_s^2)} = \mathrm{Re}\left[R^Z_{\mathcal{O}(\alpha\alpha_s^2)}\left(\frac{y_{12}\,\hat{s}}{y_{12}\,\hat{s}-\mu_Z}+\frac{(y_{34}+2y_Q)\,\hat{s}}{(y_{34}+2y_Q)\,\hat{s}-\mu_Z}\right)\right]\left(\mathrm{d}\sigma_{q\bar{q},A}\right)^{\mathrm{real}}_{\mathcal{O}(\alpha_s^3)}. \tag{A.29}$$

We emphasise that this contribution corresponds to the three-particle cuts displayed in figure 15, while real Z-boson emission of is not included in (A.29) as the Z boson is considered unstable in our calculation.

The corresponding soft function is given by

$$\left(\mathrm{d}\sigma_{q\bar{q},A}\right)^{\mathrm{soft},Z}_{\mathcal{O}(\alpha\alpha_s^2)} = \mathrm{Re}\left[R^Z_{\mathcal{O}(\alpha\alpha_s^2)}\left(\frac{2\hat{s}}{\hat{s}-\mu_Z}\right)\right]\left(\mathrm{d}\sigma_{q\bar{q},A}\right)^{\mathrm{soft}}_{\mathcal{O}(\alpha_s^3)}, \tag{A.30}$$

where the relevant QCD results can be found in (A.18) and (A.19).

The $\mathcal{O}(\alpha\alpha_s^2)$ contribution to asymmetric heavy-quark production arising from the flavour excitation process can be obtained from (A.29) by crossing. Explicitly, we have

$$\left(\mathrm{d}\sigma_{qg,A}\right)^{Z}_{\mathcal{O}(\alpha\alpha_s^2)} = \mathrm{Re}\left[R^Z_{\mathcal{O}(\alpha\alpha_s^2)}\left(\frac{y_{15}\,\hat{s}}{y_{15}\,\hat{s}+\mu_Z}+\frac{(y_{34}+2y_Q)\,\hat{s}}{(y_{34}+2y_Q)\,\hat{s}-\mu_Z}\right)\right]\left(\mathrm{d}\sigma_{qg,A}\right)_{\mathcal{O}(\alpha_s^3)}, \tag{A.31}$$

where the expression for QCD term has already been given in (A.21).

A.6 $\mathcal{O}(\alpha^2\alpha_s)$ contributions

We finally consider the corrections of $\mathcal{O}(\alpha^2\alpha_s)$, which correspond to QCD corrections to the contributions of $\mathcal{O}(\alpha^2)$ provided in (A.12). Due to the colour structure of these corrections, they can be separated into those to either the massive final-state quarks or the massless initial-state quarks. Example diagrams are depicted in figure 16.

The relevant results for the corrections associated to final-state radiation (FSR) have been provided in [81], and may be written as

$$\begin{aligned}\left(\mathrm{d}\sigma_{q\bar{q},A}\right)^{\mathrm{virt,FSR}}_{\mathcal{O}(\alpha^2\alpha_s)} &= \left(F^{\mathrm{virt}}_{\mathcal{O}(\alpha_s)}+2\delta Z^Q_{\mathcal{O}(\alpha_s)}\right)\left(\mathrm{d}\sigma_{q\bar{q},A}\right)_{\mathcal{O}(\alpha^2)}\\ &\quad+\alpha^2\alpha_s C_F\,\pi\,\frac{(\beta^2-1)\,c}{4}\,\frac{e_q e_Q a_q a_Q}{(\hat{s}-M_Z^2)^2+\Gamma_Z^2 M_Z^2}\,\Gamma_Z M_Z,\end{aligned} \tag{A.32}$$

with $C_F = 4/3$. Here $\delta Z^Q_{\mathcal{O}(\alpha_s)}$ denotes the one-loop vector QCD wave-function renormalisation constant for the heavy quark, while $F^{\mathrm{virt}}_{\mathcal{O}(\alpha_s)}$ is a form factor applied to the Born-level cross section. These quantities are given in the on-shell renormalisation scheme for the

JHEP03(2019)166

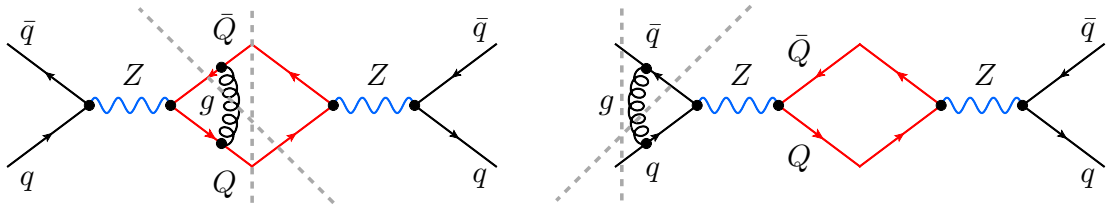

Figure 16. Possible two- and three-particle cuts that contribute to asymmetric heavy-quark production at $\mathcal{O}(\alpha^2\alpha_s)$. Graphs with photon exchange in the s-channel also give a contribution but are not explicitly shown. See text for additional details.

heavy quark by

$$\begin{aligned}
\delta Z^{Q}_{\mathcal{O}(\alpha_s)} &= -\frac{\alpha_s C_F}{2\pi}\left\{\frac{3}{2}\left[\frac{1}{\epsilon}+\ln\left(\frac{\mu^2}{m_Q^2}\right)\right]+2\right\}, \\
F^{\text{virt}}_{\mathcal{O}(\alpha^2\alpha_s)} &= \frac{\alpha_s C_F}{2\pi}\,\text{Re}\left\{-2+\left(3+\frac{1}{\beta^2}\right)B_0(m_Q^2,0,m_Q^2)\right. \\
&\quad -\left(2+\frac{1}{\beta^2}\right)B_0(\hat{s},m_Q^2,m_Q^2) \\
&\quad \left.-\hat{s}\left(1+\beta^2\right)C_0(m_Q^2,\hat{s},m_Q^2,0,m_Q^2,m_Q^2)\right\}.
\end{aligned} \tag{A.33}$$

The additional term appearing in (A.32) arises from the interference of amplitudes with Z boson and photon exchange, and is proportional to the imaginary part of the Z-boson propagator. This contribution is numerically unimportant.

The soft contribution to the FSR process takes the form

$$\left(\mathrm{d}\sigma_{q\bar{q},A}\right)^{\text{soft,FSR}}_{\mathcal{O}(\alpha^2\alpha_s)} = F^{\text{soft}}_{\mathcal{O}(\alpha^2\alpha_s)}\left(\mathrm{d}\sigma_{q\bar{q},A}\right)_{\mathcal{O}(\alpha^2)}, \tag{A.34}$$

where

$$\begin{aligned}
F^{\text{soft}}_{\mathcal{O}(\alpha^2\alpha_s)} &= \frac{\alpha_s C_F}{2\pi}\left\{\left[2+\frac{1+\beta^2}{\beta}\ln\left(\frac{1-\beta}{1+\beta}\right)\right]\left[\frac{1}{\epsilon}+2\ln\left(\frac{2E_{\text{cut}}}{\mu}\right)\right]\right. \\
&\quad \left.-\frac{1}{2\beta}\ln\left(\frac{1-\beta}{1+\beta}\right)\left[4+\left(1+\beta^2\right)\ln\left(\frac{1-\beta}{1+\beta}\right)\right]-\frac{2\left(1+\beta^2\right)}{\beta}\,\text{Li}_2\left(1-\frac{1-\beta}{1+\beta}\right)\right\},
\end{aligned} \tag{A.35}$$

with E_{cut} denoting the upper limit on the gluon energy.

For the real emission corrections from the heavy quark lines, the differential cross section reads

$$\begin{aligned}
\left(\mathrm{d}\sigma_{q\bar{q},A}\right)^{\text{real,FSR}}_{\mathcal{O}(\alpha^2\alpha_s)} &= \frac{9\alpha^2\alpha_s C_F}{16\pi N_c^2}\frac{a_q a_Q\,\hat{s}y_{12}}{\left(\hat{s}y_{12}-M_Z^2\right)^2+\Gamma_Z^2 M_Z^2} \\
&\quad\times\left[v_q v_Q+2e_q e_Q\left(1-\frac{M_Z^2}{\hat{s}y_{12}}\right)\right]f_Q,
\end{aligned} \tag{A.36}$$

JHEP03(2019)166

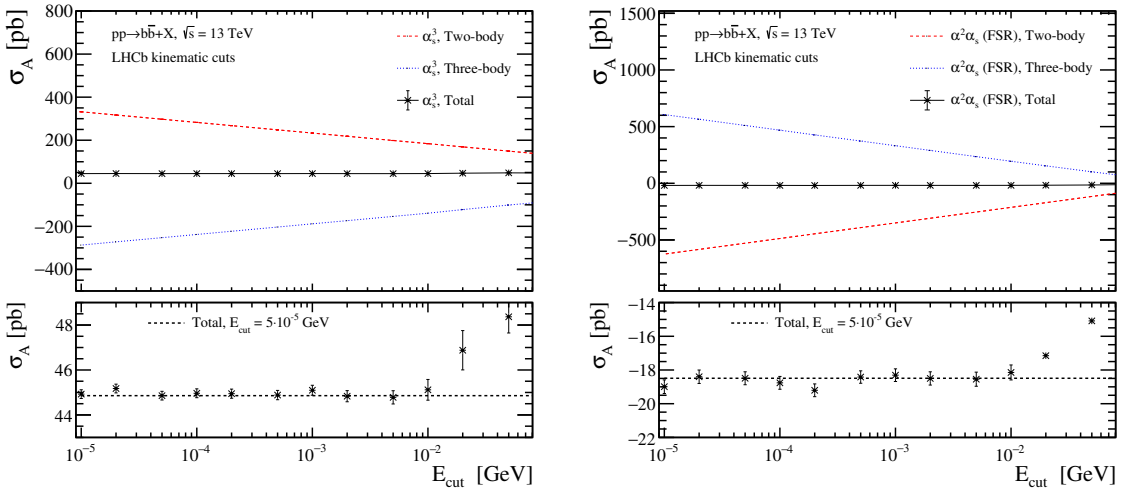

Figure 17. Dependence on the slicing parameter E_{cut} which defines the soft region of the three-body corrections. Results are shown for the asymmetric $b\bar{b}$ cross section within $m_{b\bar{b}} \in [75, 105]$ GeV, adopting the experimental selections (2.2). The left panel illustrates the $\mathcal{O}(\alpha_s^3)$ corrections, while the right panel depicts the $\mathcal{O}(\alpha^2\alpha_s)$ corrections to the massive final-state quark lines.

where the kinematic function f_Q is defined as

$$f_Q = \frac{2\,(y_{12} - y_{13} - 2y_Q) - y_{45}}{y_{35}} + \frac{2\,(y_{12} - y_{24} - 2y_Q) - y_{35}}{y_{45}} + \frac{2\,(y_{12} - 2y_{13})\,y_Q}{y_{45}^2} + \frac{2\,(y_{12} - 2y_{24})\,y_Q}{y_{35}^2} - \frac{2\,(y_{12} - y_{13} - y_{24})\,(y_{12} - 2y_Q)}{y_{35}y_{45}}\,. \tag{A.37}$$

The QCD corrections to the massless initial-state quark lines contain soft and/or collinear divergences. In this case we have chosen to provide an implementation of the $\mathcal{O}(\alpha^2\alpha_s)$ corrections using the technique of phase-space slicing [41], and performed a cross-check using dipole subtraction [42]. Rather than repeating the necessary details of both techniques, we instead refer the reader to section D of [41] for phase-space slicing, and appendix D of [42] for dipole subtraction. In the latter case, the relevant formula for the virtual correction is given in (D.9), while the general formula for the operator insertions are collected in appendix C. These relative $\mathcal{O}(\alpha_s)$ corrections can be applied to our result for the Born-level cross section of $\mathcal{O}(\alpha^2)$ provided in (A.12).

In addition to this, we provide the result for the real emission contributions to the differential cross section. They read

$$\left(\mathrm{d}\sigma_{q\bar{q},A}\right)^{\text{real,ISR}}_{\mathcal{O}(\alpha^2\alpha_s)} = \frac{9\alpha^2\alpha_s C_F}{16\pi N_c^2} \frac{a_q a_Q\,\hat{s}}{\left(\hat{s}\,(y_{34} + 2y_Q) - M_Z^2\right)^2 + \Gamma_Z^2 M_Z^2} \times \left\{ v_q v_Q\,(y_{34} + 2y_Q) + 2e_q e_Q \left[y_{34} + 2y_Q - \frac{M_Z^2}{\hat{s}} \right] \right\} f_q\,, \tag{A.38}$$

with the kinematic function f_q given by

$$f_q = \frac{1}{y_{15}y_{25}} \Big[(y_{12} - y_{15})\,(y_{12} - 2y_{13} - y_{15}) + (1 \leftrightarrow 2, 3 \leftrightarrow 4) \Big]\,. \tag{A.39}$$

JHEP03(2019)166

The cross section for the qg-initiated contributions can be obtained from crossing, and by additionally adjusting the colour averaging over the initial state.

A.7 Slicing parameter dependence

To conclude this appendix, we perform a numerical study of the dependence on the slicing parameter E_{cut} used in the phase-space slicing technique. We do this by computing the asymmetric cross section for b-quark pair production within the LHCb acceptance (2.2) for pp collisions at $\sqrt{s} = 13\,\text{TeV}$. The calculation is performed with the input parameters given in section 2.4, with factorisation and renormalisation scales set to $\mu_F = \mu_R = m_{b\bar{b}}$. The invariant mass of the b-jet pair is furthermore restricted to $m_{b\bar{b}} \in [75, 105]\,\text{GeV}$. In the left panel of figure 17 the contribution to the asymmetric cross section is shown for both the two- and three-body $\mathcal{O}(\alpha_s^3)$ contributions as well as their sum. This type of correction has been discussed in appendix A.2. In the lower panel, the y-axis is zoomed into the region around the sum of the $\mathcal{O}(\alpha_s^3)$ contributions, where the shown uncertainties are due to the accuracy of the numerical integration. A similar study is presented for the $\mathcal{O}(\alpha^2\alpha_s)$ FSR corrections discussed in appendix A.6. The corresponding results are given on the right-hand side in figure 17. The numerical results of this work employ the choice $E_{\text{cut}} = 5 \cdot 10^{-5}\,\text{GeV}$, and the NLO coefficients are obtained with a relative precision of around 1% to 2% in this case.

References

[1] ALEPH, DELPHI, L3, OPAL, SLD, LEP Electroweak Working Group, SLD Electroweak Group and SLD Heavy Flavour Group collaborations, *Precision electroweak measurements on the Z resonance*, *Phys. Rept.* **427** (2006) 257 [hep-ex/0509008] [INSPIRE].

[2] D0 collaboration, *Measurement of the forward-backward asymmetry in the production of $B^{\pm}$ mesons in $p\bar{p}$ collisions at $\sqrt{s} = 1.96$ TeV*, *Phys. Rev. Lett.* **114** (2015) 051803 [arXiv:1411.3021] [INSPIRE].

[3] CDF collaboration, *Measurement of the forward-backward asymmetry in low-mass bottom-quark pairs produced in proton-antiproton collisions*, *Phys. Rev.* **D 93** (2016) 112003 [arXiv:1601.06526] [INSPIRE].

[4] LHCb collaboration, *First measurement of the charge asymmetry in beauty-quark pair production*, *Phys. Rev. Lett.* **113** (2014) 082003 [arXiv:1406.4789] [INSPIRE].

[5] Y. Bai, J.L. Hewett, J. Kaplan and T.G. Rizzo, *LHC predictions from a Tevatron anomaly in the top quark forward-backward asymmetry*, *JHEP* **03** (2011) 003 [arXiv:1101.5203] [INSPIRE].

[6] D. Kahawala, D. Krohn and M.J. Strassler, *Measuring the bottom-quark forward-central asymmetry at the LHC*, *JHEP* **01** (2012) 069 [arXiv:1108.3301] [INSPIRE].

[7] P. Saha, *Bottom pair production and search for heavy resonances*, *Phys. Lett.* **B 700** (2011) 221 [arXiv:1101.5797] [INSPIRE].

[8] A.V. Manohar and M. Trott, *Electroweak Sudakov corrections and the top quark forward-backward asymmetry*, *Phys. Lett.* **B 711** (2012) 313 [arXiv:1201.3926] [INSPIRE].

JHEP03(2019)166

[9] J. Drobnak, J.F. Kamenik and J. Zupan, *Flipping $t\bar{t}$ asymmetries at the Tevatron and the LHC*, *Phys. Rev.* **D 86** (2012) 054022 [arXiv:1205.4721] [INSPIRE].

[10] C. Delaunay, O. Gedalia, Y. Hochberg and Y. Soreq, *Predictions from heavy new physics interpretation of the top forward-backward asymmetry*, *JHEP* **12** (2012) 053 [arXiv:1207.0740] [INSPIRE].

[11] S. Ipek, *Light axigluon contributions to $b\bar{b}$ and $c\bar{c}$ asymmetry and constraints on flavor changing axigluon currents*, *Phys. Rev.* **D 87** (2013) 116010 [arXiv:1301.3990] [INSPIRE].

[12] B. Grinstein and C.W. Murphy, *Bottom-quark forward-backward asymmetry in the Standard Model and beyond*, *Phys. Rev. Lett.* **111** (2013) 062003 [*Erratum ibid.* **112** (2014) 239901] [arXiv:1302.6995] [INSPIRE].

[13] C.W. Murphy, *Bottom-quark forward-backward and charge asymmetries at hadron colliders*, *Phys. Rev.* **D 92** (2015) 054003 [arXiv:1504.02493] [INSPIRE].

[14] R. Gauld, U. Haisch, B.D. Pecjak and E. Re, *Beauty-quark and charm-quark pair production asymmetries at LHCb*, *Phys. Rev.* **D 92** (2015) 034007 [arXiv:1505.02429] [INSPIRE].

[15] LHCb collaboration, *The LHCb detector at the LHC*, 2008 *JINST* **3** S08005 [INSPIRE].

[16] LHCb collaboration, *Identification of beauty and charm quark jets at LHCb*, 2015 *JINST* **10** P06013 [arXiv:1504.07670] [INSPIRE].

[17] LHCb collaboration, *First observation of forward $Z \to b\bar{b}$ production in pp collisions at $\sqrt{s} = 8$ TeV*, *Phys. Lett.* **B 776** (2018) 430 [arXiv:1709.03458] [INSPIRE].

[18] M. Cacciari, G.P. Salam and G. Soyez, *The anti-k_t jet clustering algorithm*, *JHEP* **04** (2008) 063 [arXiv:0802.1189] [INSPIRE].

[19] J.C. Collins, D.E. Soper and G.F. Sterman, *Factorization of hard processes in QCD*, *Adv. Ser. Direct. High Energy Phys.* **5** (1989) 1 [hep-ph/0409313] [INSPIRE].

[20] P. Nason, S. Dawson and R.K. Ellis, *The total cross-section for the production of heavy quarks in hadronic collisions*, *Nucl. Phys.* **B 303** (1988) 607 [INSPIRE].

[21] P. Nason, S. Dawson and R.K. Ellis, *The one particle inclusive differential cross-section for heavy quark production in hadronic collisions*, *Nucl. Phys.* **B 327** (1989) 49 [*Erratum ibid.* **B 335** (1990) 260] [INSPIRE].

[22] M.L. Mangano, P. Nason and G. Ridolfi, *Heavy quark correlations in hadron collisions at next-to-leading order*, *Nucl. Phys.* **B 373** (1992) 295 [INSPIRE].

[23] W. Beenakker, W.L. van Neerven, R. Meng, G.A. Schuler and J. Smith, *QCD corrections to heavy quark production in hadron hadron collisions*, *Nucl. Phys.* **B 351** (1991) 507 [INSPIRE].

[24] W. Beenakker, H. Kuijf, W.L. van Neerven and J. Smith, *QCD corrections to heavy quark production in $p\bar{p}$ collisions*, *Phys. Rev.* **D 40** (1989) 54 [INSPIRE].

[25] J.H. Kühn, A. Scharf and P. Uwer, *Electroweak corrections to top-quark pair production in quark-antiquark annihilation*, *Eur. Phys. J.* **C 45** (2006) 139 [hep-ph/0508092] [INSPIRE].

[26] J.H. Kühn, A. Scharf and P. Uwer, *Electroweak effects in top-quark pair production at hadron colliders*, *Eur. Phys. J.* **C 51** (2007) 37 [hep-ph/0610335] [INSPIRE].

[27] W. Bernreuther, M. Fücker and Z.-G. Si, *Weak interaction corrections to hadronic top quark pair production*, *Phys. Rev.* **D 74** (2006) 113005 [hep-ph/0610334] [INSPIRE].

[28] W. Hollik and M. Kollar, *NLO QED contributions to top-pair production at hadron collider*, *Phys. Rev.* **D 77** (2008) 014008 [arXiv:0708.1697] [INSPIRE].

JHEP03(2019)166

[29] J.H. Kühn, A. Scharf and P. Uwer, *Weak effects in b-jet production at hadron colliders*, *Phys. Rev.* **D 82** (2010) 013007 [arXiv:0909.0059] [INSPIRE].

[30] A. Buckley et al., *LHAPDF6: parton density access in the LHC precision era*, *Eur. Phys. J.* **C 75** (2015) 132 [arXiv:1412.7420] [INSPIRE].

[31] T. Hahn, *CUBA: a library for multidimensional numerical integration*, *Comput. Phys. Commun.* **168** (2005) 78 [hep-ph/0404043] [INSPIRE].

[32] A. van Hameren, C.G. Papadopoulos and R. Pittau, *Automated one-loop calculations: a proof of concept*, *JHEP* **09** (2009) 106 [arXiv:0903.4665] [INSPIRE].

[33] A. van Hameren, *OneLOop: for the evaluation of one-loop scalar functions*, *Comput. Phys. Commun.* **182** (2011) 2427 [arXiv:1007.4716] [INSPIRE].

[34] S. Frixione, P. Nason and G. Ridolfi, *A positive-weight next-to-leading-order Monte Carlo for heavy flavour hadroproduction*, *JHEP* **09** (2007) 126 [arXiv:0707.3088] [INSPIRE].

[35] V. Hirschi, R. Frederix, S. Frixione, M.V. Garzelli, F. Maltoni and R. Pittau, *Automation of one-loop QCD corrections*, *JHEP* **05** (2011) 044 [arXiv:1103.0621] [INSPIRE].

[36] V. Hirschi and O. Mattelaer, *Automated event generation for loop-induced processes*, *JHEP* **10** (2015) 146 [arXiv:1507.00020] [INSPIRE].

[37] J. Alwall et al., *The automated computation of tree-level and next-to-leading order differential cross sections and their matching to parton shower simulations*, *JHEP* **07** (2014) 079 [arXiv:1405.0301] [INSPIRE].

[38] *Computing the interference of loop-induced diagrams with a tree-level background with MadEvent in MG5aMC webpage*, https://cp3.irmp.ucl.ac.be/projects/madgraph/wiki/LoopInducedTimesTree.

[39] T. Hahn, *Generating Feynman diagrams and amplitudes with FeynArts* 3, *Comput. Phys. Commun.* **140** (2001) 418 [hep-ph/0012260] [INSPIRE].

[40] T. Hahn and M. Pérez-Victoria, *Automatized one loop calculations in four-dimensions and D-dimensions*, *Comput. Phys. Commun.* **118** (1999) 153 [hep-ph/9807565] [INSPIRE].

[41] B.W. Harris and J.F. Owens, *The two cutoff phase space slicing method*, *Phys. Rev.* **D 65** (2002) 094032 [hep-ph/0102128] [INSPIRE].

[42] S. Catani and M.H. Seymour, *A general algorithm for calculating jet cross-sections in NLO QCD*, *Nucl. Phys.* **B 485** (1997) 291 [*Erratum ibid.* **B 510** (1998) 503] [hep-ph/9605323] [INSPIRE].

[43] M. Czakon, P. Fiedler and A. Mitov, *Resolving the Tevatron top quark forward-backward asymmetry puzzle: fully differential next-to-next-to-leading-order calculation*, *Phys. Rev. Lett.* **115** (2015) 052001 [arXiv:1411.3007] [INSPIRE].

[44] J. Currie, E.W.N. Glover and J. Pires, *Next-to-next-to leading order QCD predictions for single jet inclusive production at the LHC*, *Phys. Rev. Lett.* **118** (2017) 072002 [arXiv:1611.01460] [INSPIRE].

[45] LHC Higgs Cross Section Working Group collaboration, *Handbook of LHC Higgs cross sections: 4. Deciphering the nature of the Higgs sector*, arXiv:1610.07922 [INSPIRE].

[46] A. Manohar, P. Nason, G.P. Salam and G. Zanderighi, *How bright is the proton? A precise determination of the photon parton distribution function*, *Phys. Rev. Lett.* **117** (2016) 242002 [arXiv:1607.04266] [INSPIRE].

JHEP03(2019)166

[47] A. Banfi, G.P. Salam and G. Zanderighi, *Infrared safe definition of jet flavor*, *Eur. Phys. J.* **C 47** (2006) 113 [hep-ph/0601139] [INSPIRE].

[48] M. Czakon, P. Fiedler and A. Mitov, *Total top-quark pair-production cross section at hadron colliders through $O(\alpha_S^4)$*, *Phys. Rev. Lett.* **110** (2013) 252004 [arXiv:1303.6254] [INSPIRE].

[49] NNPDF collaboration, *Parton distributions from high-precision collider data*, *Eur. Phys. J.* **C 77** (2017) 663 [arXiv:1706.00428] [INSPIRE].

[50] M. Cacciari, M. Greco and P. Nason, *The p_T spectrum in heavy flavor hadroproduction*, *JHEP* **05** (1998) 007 [hep-ph/9803400] [INSPIRE].

[51] D. de Florian, G.F.R. Sborlini and G. Rodrigo, *QED corrections to the Altarelli-Parisi splitting functions*, *Eur. Phys. J.* **C 76** (2016) 282 [arXiv:1512.00612] [INSPIRE].

[52] L.A. Harland-Lang, V.A. Khoze and M.G. Ryskin, *The photon PDF in events with rapidity gaps*, *Eur. Phys. J.* **C 76** (2016) 255 [arXiv:1601.03772] [INSPIRE].

[53] L.A. Harland-Lang, V.A. Khoze and M.G. Ryskin, *Photon-initiated processes at high mass*, *Phys. Rev.* **D 94** (2016) 074008 [arXiv:1607.04635] [INSPIRE].

[54] A.V. Manohar, P. Nason, G.P. Salam and G. Zanderighi, *The photon content of the proton*, *JHEP* **12** (2017) 046 [arXiv:1708.01256] [INSPIRE].

[55] NNPDF collaboration, *Illuminating the photon content of the proton within a global PDF analysis*, *SciPost Phys.* **5** (2018) 008 [arXiv:1712.07053] [INSPIRE].

[56] D. Pagani, I. Tsinikos and M. Zaro, *The impact of the photon PDF and electroweak corrections on $t\bar{t}$ distributions*, *Eur. Phys. J.* **C 76** (2016) 479 [arXiv:1606.01915] [INSPIRE].

[57] M. Czakon, D. Heymes, A. Mitov, D. Pagani, I. Tsinikos and M. Zaro, *Top-pair production at the LHC through NNLO QCD and NLO EW*, *JHEP* **10** (2017) 186 [arXiv:1705.04105] [INSPIRE].

[58] M. Czakon, D. Heymes, A. Mitov, D. Pagani, I. Tsinikos and M. Zaro, *Top-quark charge asymmetry at the LHC and Tevatron through NNLO QCD and NLO EW*, *Phys. Rev.* **D 98** (2018) 014003 [arXiv:1711.03945] [INSPIRE].

[59] J. Fleischer, O.V. Tarasov and F. Jegerlehner, *Two loop heavy top corrections to the ρ parameter: a simple formula valid for arbitrary Higgs mass*, *Phys. Lett.* **B 319** (1993) 249 [INSPIRE].

[60] A. Denner, S. Dittmaier, M. Roth and L.H. Wieders, *Electroweak corrections to charged-current $e^+e^- \to 4$ fermion processes: technical details and further results*, *Nucl. Phys.* **B 724** (2005) 247 [*Erratum ibid.* **B 854** (2012) 504] [hep-ph/0505042] [INSPIRE].

[61] A.L. Kagan, J.F. Kamenik, G. Perez and S. Stone, *Top LHCb physics*, *Phys. Rev. Lett.* **107** (2011) 082003 [arXiv:1103.3747] [INSPIRE].

[62] R. Gauld, *Feasibility of top quark measurements at LHCb and constraints on the large-x gluon PDF*, *JHEP* **02** (2014) 126 [arXiv:1311.1810] [INSPIRE].

[63] R. Gauld, *Leptonic top-quark asymmetry predictions at LHCb*, *Phys. Rev.* **D 91** (2015) 054029 [arXiv:1409.8631] [INSPIRE].

[64] LHCb collaboration, *First observation of top quark production in the forward region*, *Phys. Rev. Lett.* **115** (2015) 112001 [arXiv:1506.00903] [INSPIRE].

[65] LHCb collaboration, *Measurement of forward top pair production in the dilepton channel in pp collisions at $\sqrt{s} = 13$ TeV*, *JHEP* **08** (2018) 174 [arXiv:1803.05188] [INSPIRE].

JHEP03(2019)166

[66] M. Czakon et al., *Resummation for (boosted) top-quark pair production at NNLO+NNLL' in QCD*, *JHEP* **05** (2018) 149 [arXiv:1803.07623] [INSPIRE].

[67] LHCb collaboration, *Physics case for an LHCb upgrade II — opportunities in flavour physics and beyond, in the HL-LHC era*, arXiv:1808.08865 [INSPIRE].

[68] D. Liu, J. Liu, C.E.M. Wagner and X.-P. Wang, *Bottom-quark forward-backward asymmetry, dark matter and the LHC*, *Phys. Rev.* **D 97** (2018) 055021 [arXiv:1712.05802] [INSPIRE].

[69] A.B. Arbuzov et al., *ZFITTER: a semi-analytical program for fermion pair production in e^+e^- annihilation, from version* 6.21 *to version* 6.42, *Comput. Phys. Commun.* **174** (2006) 728 [hep-ph/0507146] [INSPIRE].

[70] PARTICLE DATA GROUP collaboration, *Review of particle physics*, *Phys. Rev.* **D 98** (2018) 030001 [INSPIRE].

[71] CMS collaboration, *Search for low mass vector resonances decaying into quark-antiquark pairs in proton-proton collisions at $\sqrt{s} = 13$ TeV*, *JHEP* **01** (2018) 097 [arXiv:1710.00159] [INSPIRE].

[72] ATLAS collaboration, *Search for the neutral Higgs bosons of the minimal supersymmetric Standard Model in pp collisions at $\sqrt{s} = 7$ TeV with the ATLAS detector*, *JHEP* **02** (2013) 095 [arXiv:1211.6956] [INSPIRE].

[73] ATLAS collaboration, *Search for new high-mass phenomena in the dilepton final state using 36 fb^{-1} of proton-proton collision data at $\sqrt{s} = 13$ TeV with the ATLAS detector*, *JHEP* **10** (2017) 182 [arXiv:1707.02424] [INSPIRE].

[74] P. Schwaller, D. Stolarski and A. Weiler, *Emerging jets*, *JHEP* **05** (2015) 059 [arXiv:1502.05409] [INSPIRE].

[75] U. Haisch and J.F. Kamenik, *Searching for new spin-0 resonances at LHCb*, *Phys. Rev.* **D 93** (2016) 055047 [arXiv:1601.05110] [INSPIRE].

[76] P. Ilten, Y. Soreq, J. Thaler, M. Williams and W. Xue, *Proposed inclusive dark photon search at LHCb*, *Phys. Rev. Lett.* **116** (2016) 251803 [arXiv:1603.08926] [INSPIRE].

[77] LHCb collaboration, *Search for dark photons produced in 13 TeV pp collisions*, *Phys. Rev. Lett.* **120** (2018) 061801 [arXiv:1710.02867] [INSPIRE].

[78] P. Ilten, Y. Soreq, M. Williams and W. Xue, *Serendipity in dark photon searches*, *JHEP* **06** (2018) 004 [arXiv:1801.04847] [INSPIRE].

[79] U. Haisch, J.F. Kamenik, A. Malinauskas and M. Spira, *Collider constraints on light pseudoscalars*, *JHEP* **03** (2018) 178 [arXiv:1802.02156] [INSPIRE].

[80] LHCb collaboration, *Search for a dimuon resonance in the Υ mass region*, *JHEP* **09** (2018) 147 [arXiv:1805.09820] [INSPIRE].

[81] J. Jersak, E. Laermann and P.M. Zerwas, *Electroweak production of heavy quarks in e^+e^- annihilation*, *Phys. Rev.* **D 25** (1982) 1218 [*Erratum ibid.* **D 36** (1987) 310] [INSPIRE].

[82] W. Hollik and D. Pagani, *The electroweak contribution to the top quark forward-backward asymmetry at the Tevatron*, *Phys. Rev.* **D 84** (2011) 093003 [arXiv:1107.2606] [INSPIRE].

[83] J.H. Kühn and G. Rodrigo, *Charge asymmetry of heavy quarks at hadron colliders*, *Phys. Rev.* **D 59** (1999) 054017 [hep-ph/9807420] [INSPIRE].

JHEP03(2019)166